Research Square

Preprints are preliminary reports that have not undergone peer review.
They should not be considered conclusive, used to inform clinical practice,
or referenced by the media as validated information.

Modeling of Rayleigh-type waves in a viscoelastic piezoelectric fiber-reinforced composite layered Structure

Bikram Dholey
Jadavpur University
Kshitish Ch. Mistri
kchmistri@gmail.com
Ramakrishna Mission Vivekananda Centenary College
Amrita Das
Polba Mahavidyalaya
Gopal Chandra Shit
Jadavpur University

Research Article

Keywords: Rayleigh-type wave, Viscoelastic piezoelectric fiber-reinforced composite (VRFRC), Imperfect interface, Rule of mixtures, Viscous relaxation time, Attenuation

Posted Date: October 30th, 2026

DOI: https://doi.org/10.21203/rs.3.rs-11359181/v1

License: This work is licensed under a Creative Commons Attribution 4.0 International License.
Read Full License

Additional Declarations: No competing interests reported.

Modeling of Rayleigh-type waves in a viscoelastic piezoelectric fiber-reinforced composite layered Structure

Bikram Dholey[a], Kshitish Ch. Mistri[b,*], Amrita Das[c], Gopal Chandra Shit[a]

[a]*Department of Mathematics, Jadavpur University, Kolkata, West Bengal, India*
[b]*Department of Mathematics, Ramakrishna Mission Vivekananda Centenary College, Rahara, India*
[c]*Department of Mathematics, Polba Mahavidyalaya, Polba, Hooghly, West Bengal, India*

Abstract

The propagation of Rayleigh-type surface waves in a viscoelastic piezoelectric fiber-reinforced composite (VRFRC) layer bonded to an isotropic elastic half-space through a mechanically imperfect interface is investigated. Both constituents of the composite are dissipative: the PZT fibers are treated as viscoelastic piezoelectric solids and the epoxy matrix as a viscoelastic dielectric, each described by Kelvin–Voigt elements acting on the stress–strain and on the electric field–electric displacement pairs, so that every phase, and the homogenized composite, is passive. The complex, frequency-dependent effective constants are obtained by introducing the complex constituent constants into the strength-of-materials/rule-of-mixtures (SM/RM) relations through the elastic–viscoelastic correspondence principle. The imperfect bond is represented by normal and tangential linear-slip conditions, the upper surface is traction-free and electrically open, and the metallic substrate grounds the interface. An exact 8×8 complex dispersion relation is derived and solved, without any small-loss approximation, for the phase velocity and the normalized attenuation of the fundamental mode. The results show that the fiber volume fraction controls the dispersion through the layer stiffness and piezoelectric stiffening, the viscous relaxation times of the matrix (chiefly $\eta_{33}^{c,q}$ and $\eta_{44}^{c,q}$) control the attenuation while leaving the phase velocity almost unchanged, fiber viscoelasticity becomes significant only at high fiber content, and interfacial compliance, in particular the normal compliance, lowers the phase velocity and the attenuation in the dispersive range. Mode shapes, particle orbits, the electric potential distribution and a velocity-based electromechanical coupling measure are also analysed; the group velocity shows a pronounced Airy-phase minimum that is sensitive to the fiber content and the bond quality, and the velocity-based coupling measure $K^2 = 2(c_{\text{open}} - c_{\text{short}})/c_{\text{open}}$ reaches about 3.3% for fiber-rich layers.

Keywords: Rayleigh-type wave, Viscoelastic piezoelectric fiber-reinforced composite (VRFRC), Imperfect interface, Rule of mixtures, Viscous relaxation time, Attenuation

1. Introduction

The integration of functional phases into fiber-reinforced composites has generated a class of multifunctional materials capable of combining structural load-bearing capacity with sensing and actuation functionalities. Fiber-reinforced composites (FRCs) are particularly desirable because their stiffness, strength-to-weight ratio, and direc-

*Corresponding Author.
Email address: kchmistri@gmail.com (Kshitish Ch. Mistri)

tional mechanical response may be tuned by fiber selection and microstructural design. These properties have encouraged their application in aeronautical structures, transportation systems, civic infrastructure, and smart engineering gadgets. A further increase is accomplished by integrating piezoelectric elements into the composite architecture, leading to piezoelectric fiber-reinforced composites (PFRCs). Such materials have an intrinsic electromechanical coupling mechanism by which mechanical deformation can be turned into an electrical reaction and vice versa. Consequently, PFRCs have emerged as promising candidates for structural sensing, energy harvesting, active vibration suppression, and integrated actuation, while preserving many of the load-bearing characteristics of conventional composite materials [1–6]. The electromechanical response of these composites is strongly dependent on constituent proportions and microstructural characteristics, and recent investigations have demonstrated that appropriate control of the piezoelectric phase and reinforcement architecture can substantially modify their effective properties [7, 8]. At the same time, the propagation and detection of stress waves in advanced composite structures have become increasingly important for the development of reliable structural health-monitoring systems and for understanding the role of reinforcement and interfaces in wave transmission [9, 10].

An additional level of complication develops when the polymeric elements display viscoelastic activity. In actual composite materials, the polymer matrix is intrinsically dissipative, and its mechanical response depends on both the excitation frequency and the distinctive relaxation processes of the constituent material [11]. Under harmonic stimulation, this behavior may simply be represented by complex-valued constitutive parameters, with their real and imaginary components representing the storage and dissipative qualities of the material, respectively [12]. A physically admissible representation must satisfy the passivity criterion so that the modeled medium dissipates mechanical energy rather than generates it. Similar considerations emerge in piezoelectric ceramics, where elastic, dielectric, and piezoelectric losses may contribute to the overall electromechanical dissipation and consequently necessitate a thermodynamically consistent complex-parameter formulation [13]. The simultaneous presence of piezoelectric coupling and viscoelastic dissipation therefore provides a substantially frequency-dependent electromechanical response. Such properties are particularly significant to wave propagation since material losses influence not only the phase velocity but also the attenuation and dispersion of guided and surface waves [14, 15]. These qualities stimulate the consideration of piezoelectric–viscoelastic fiber-reinforced composites (VRFRCs) as realistic multifunctional media for wave-based sensing and monitoring applications.

Surface-wave propagation in heterogeneous solids has likewise garnered sustained attention owing to its significance to nondestructive characterization, geophysical exploration, wave-based sensing, and smart structural systems. In particular, Rayleigh-type waves are particularly sensitive to the material properties and near-surface conditions of layered media, making them helpful for detecting variations in material composition and interfacial characteristics [16, 17]. Previous investigations have proven that material inhomogeneity, functional gradation, prestress, and foundation effects can greatly modify the dispersion characteristics of Rayleigh waves [18–20]. When the host medium possesses electromechanical coupling, the surface-wave response becomes extra dependent on the interaction between mechanical deformation and the electric field. This interaction, combined with interface flaws, can dramatically affect wave speed, mode properties, and energy transfer in piezoelectric and fiber-reinforced structures [21–23]. More elaborate formulations incorporating prestress, rotation, and coupled thermal, electrical, and mechanical fields have further demonstrated that multiphysics interactions can produce significant changes in wave reflection, transmission, and dispersion [24–28]. In parallel, formulations based on functionally graded, micropolar, nonlocal, and metasurface theories have revealed additional mechanisms for controlling surface-wave propagation and generating unconven-

tional dispersion characteristics [29–31]. Related research on shear, torsional, and cylindrical surface-wave propagation have also provided useful insight into wave behavior in multilayer and geometrically complicated multifunctional structures [32–36].

For most actual applications, however, the notion of a completely bonded interface is an idealization. Piezoelectric composite layers are often deposited, bonded, or linked to a host substrate through an adhesive or mechanically compliant interphase, whose finite stiffness can facilitate relative displacement between the adjoining media. Ignoring this interfacial compliance may consequently lead to erroneous estimates of surface-wave properties, particularly when the wavelength becomes similar with the characteristic dimensions of the interfacial region. A widely adopted representation of such imperfect bonding is the linear spring or linear-slip model, in which the traction remains continuous while the displacement discontinuity across the interface is related to the corresponding traction through an interfacial stiffness parameter [37–39]. This framework has subsequently been employed to investigate SH, Love, torsional, and related wave modes in piezoelectric and fiber-reinforced layered structures [33, 40–44], as well as Rayleigh-wave propagation across imperfectly bonded piezoelectric bimaterials [21]. These investigations illustrate the importance of interfacial compliance; yet, the combined influence of bulk viscoelastic dissipation and poor bonding remains little investigated for piezoelectric fiber-reinforced surface-wave systems.

In particular, there is a distinct gap in the existing literature concerning Rayleigh-type wave propagation in a viscoelastic piezoelectric fiber-reinforced composite layer in which both the reinforcing fibers and the polymeric matrix exhibit viscoelastic behavior, while the composite is coupled to an elastic substrate through an imperfect interface. This design is significant because the two viscoelastic parts can contain different relaxation characteristics, and their combined influence cannot, in general, be described satisfactorily by assigning dissipation exclusively to the matrix. Moreover, the interfacial compliance offers an additional mechanism of wave-energy redistribution and attenuation. A comprehensive treatment of these factors is therefore important to elucidate the combined roles of constituent viscoelasticity, fiber concentration, and interface stiffness in determining the complicated dispersion properties of surface waves.

Motivated by this gap, the present study presents an analytical electromechanical framework for Rayleigh-type wave propagation in an imperfectly bonded VRFRC layer across an elastic half-space. Viscoelastic effects in both constituent phases are integrated using passive Kelvin–Voigt-type complex material characteristics, while the effective electromechanical properties of the composite are evaluated using the proposed self-consistent/mixing relations. The VRFRC layer is subsequently linked to the elastic substrate by independent normal and tangential interfacial spring compliances, so allowing the influence of imperfect bonding to be evaluated without imposing the restrictive assumption of perfect continuity. The ensuing boundary-value issue leads to a sophisticated dispersion equation from which both the phase velocity and attenuation properties are determined. The concept is further evaluated through appropriate limiting situations to show its agreement with recognized theoretical models. Particular focus is dedicated to measuring the impacts of fiber volume fraction, the relaxation periods associated with the matrix and fiber phases, and the normal and tangential interfacial stiffnesses. The resulting study provides a systematic framework for examining how bulk viscoelasticity and poor interfacial bonding together regulate surface-wave dispersion and attenuation in multifunctional piezoelectric composite materials.

2. Model Formulation

2.1. Geometry of the model

A VRFRC layer of thickness h occupies $0 \le z \le h$ and rests on an isotropic elastic half-space $z \ge h$ (Fig. 1). The fibers are aligned with the propagation direction x ($= x_1$), the composite is poled along z ($= x_3$), and a Rayleigh-type wave propagates along x with motion in the sagittal x–z plane. The upper surface $z = 0$ is traction-free and electrically open, and the layer is attached to the substrate through an imperfect (spring-type) interface at $z = h$. The substrate is a metal (aluminium), so that the interface acts as a grounded electrode.

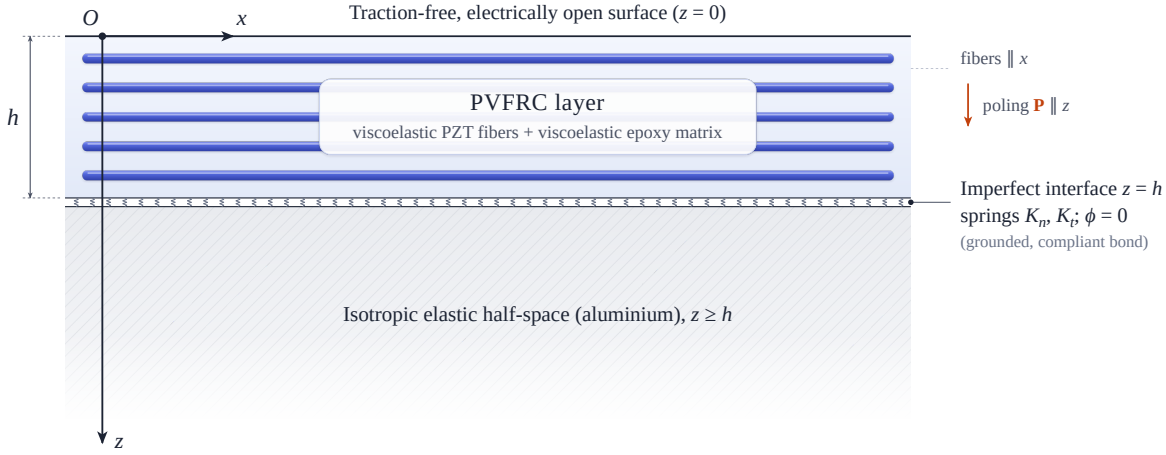


Fig. 1. VRFRC layer imperfectly bonded to an isotropic elastic half-space. The fibers are aligned with the propagation direction x; the interface is represented by normal (K_n) and tangential (K_t) springs.

2.2. Micro-mechanical VRFRC media with viscoelastic fibers and matrix

The VRFRC consists of PZT-5A fibers embedded in an epoxy matrix. In contrast to conventional PFRC descriptions, dissipation is present in both constituents: the fibers are viscoelastic piezoelectric solids, and the matrix is a viscoelastic, piezoelectrically inert dielectric. Throughout, the constitutive equations are written in the stress–charge form, with strain s_{ij} and electric field $E_i = -\partial\phi/\partial x_i$ as independent variables. For phase $r \in \{f, q\}$ (fiber, matrix) the losses are represented by Kelvin–Voigt elements [12, 13]: a dashpot in parallel with each elastic spring, and a dielectric relaxation acting on the free part $D_i - e_{ikl}s_{kl}$ of the electric displacement,

$$\tau^r_{ij} = c'^r_{ijkl}\left(s^r_{kl} + \eta^{c,r}_{ijkl}\,\dot{s}^r_{kl}\right) - e^r_{kij}E_k, \qquad \left(1 + \eta^{\varepsilon,r}_{ik}\,\frac{\partial}{\partial t}\right)\left(D^r_i - e^r_{ilm}s^r_{lm}\right) = \varepsilon'^r_{ik}E_k \tag{1}$$

(no summation over the indices of η), where c'^r_{ijkl}, e^r_{kij} and ε'^r_{ik} are the elastic, piezoelectric and dielectric constants of the instantaneous response and $\eta^{c,r}$, $\eta^{\varepsilon,r}$ are viscous relaxation times (unit: s). The same piezoelectric tensor e appears in both equations, so that the direct and converse effects are described consistently. For time-harmonic fields $\propto e^{-i\omega t}$, Eq. (1) reduces to the elastic form with the complex constituent constants

$$c^r_{ij} = c'^r_{ij} - i\omega c''^r_{ij} = c'^r_{ij}(1 - i\omega\eta^{c,r}_{ij}), \qquad \varepsilon^r_{ij} = \frac{\varepsilon'^r_{ij}}{1 - i\omega\eta^{\varepsilon,r}_{ij}}, \qquad e^f_{ij} = e'^f_{ij}(1 - i\omega\eta^{e,f}_{ij}), \qquad e^q_{ij} = 0, \tag{2}$$

where $\eta^{c,r}_{ij} = c''^{r}_{ij}/c'^{r}_{ij}$ and $\eta^{\varepsilon,r}_{ij}$ are the viscous relaxation times of the stiffness and of the permittivity, and $\omega\eta^{c,r}_{ij}$, $\omega\eta^{\varepsilon,r}_{ij}$ are the dimensionless internal-friction (loss-tangent) parameters [11, 45, 46]; they are proportional to the frequency. A piezoelectric loss with relaxation time $\eta^{e,f}_{ij}$ is allowed for generality; it is set to zero in the computations, so that e^{f}_{ij} is real. With the time dependence $e^{-i\omega t}$, the time-averaged power absorbed per unit volume in the x–z problem is non-negative if and only if the loss matrix

$$\mathbf{L} = \begin{bmatrix} -\operatorname{Im}\mathbf{C} & (\operatorname{Im}\mathbf{e})^{T} \\ \operatorname{Im}\mathbf{e} & \operatorname{Im}\boldsymbol{\varepsilon} \end{bmatrix} \tag{3}$$

is positive semi-definite. Two forms of $\mathbf{L}$ are used. For each constituent, $\mathbf{C}$ (6×6, Voigt strains), $\mathbf{e}$ (3×6) and $\boldsymbol{\varepsilon}$ (3×3) are the complete matrices of Eqs. (4)–(7), so that $\mathbf{L}$ (9×9) is the complete coupled dissipation matrix of the generalized variables $(\mathbf{s},\mathbf{E})$. For the homogenized medium in the sagittal problem, the generalized variables are $(s_{11}, s_{33}, 2s_{13}, E_1, E_3)$ and $\mathbf{L}$ is 5×5. Eq. (2) gives $\operatorname{Im} c_{ii} < 0$ and $\operatorname{Im}\varepsilon_{ii} > 0$. This is necessary but not sufficient: the elastic block of $\mathbf{L}$ is $\omega[c'_{IJ}\eta^{c}_{IJ}]$, and it is positive semi-definite for equal relaxation times ($\eta^{c}_{IJ} = \eta$, since $[c'_{IJ}]$ is positive definite) but not for arbitrary independent relaxation times. For example, for the epoxy matrix with all other relaxation times equal to 10 ns, $[c'_{IJ}\eta^{c}_{IJ}]$ is positive semi-definite only for $0 \le \eta^{c,q}_{13} \le 15.02$ ns; $\eta^{c,q}_{13} = 20$ ns would describe an active (energy-generating) matrix. Every relaxation-time set used in this paper was therefore checked individually (Table 3). Note that the form $\varepsilon' - i\omega\varepsilon'' = \varepsilon'(1 - i\omega\eta^{\varepsilon})$, which follows from $D = \varepsilon' E + \varepsilon'' \dot{E}$, has $\operatorname{Im}\varepsilon < 0$ for $e^{-i\omega t}$ and describes an energy-generating dielectric; the dielectric relaxation is therefore written as in Eq. (1). To first order in $\omega\eta^{\varepsilon}$ both forms have the same storage part, $\operatorname{Re}\varepsilon \approx \varepsilon'$, but the loss parts have opposite signs.

The constitutive relations of the viscoelastic piezoelectric fibers in the frequency domain are [4, 47]

$$\begin{bmatrix} \tau^{f}_{11} \\ \tau^{f}_{22} \\ \tau^{f}_{33} \\ \tau^{f}_{23} \\ \tau^{f}_{13} \\ \tau^{f}_{12} \end{bmatrix} = \begin{bmatrix} c^{f}_{11} & c^{f}_{12} & c^{f}_{13} & 0 & 0 & 0 \\ c^{f}_{12} & c^{f}_{22} & c^{f}_{23} & 0 & 0 & 0 \\ c^{f}_{13} & c^{f}_{23} & c^{f}_{33} & 0 & 0 & 0 \\ 0 & 0 & 0 & c^{f}_{44} & 0 & 0 \\ 0 & 0 & 0 & 0 & c^{f}_{55} & 0 \\ 0 & 0 & 0 & 0 & 0 & c^{f}_{66} \end{bmatrix} \begin{bmatrix} s^{f}_{11} \\ s^{f}_{22} \\ s^{f}_{33} \\ 2s^{f}_{23} \\ 2s^{f}_{13} \\ 2s^{f}_{12} \end{bmatrix} - \begin{bmatrix} 0 & 0 & e^{f}_{31} \\ 0 & 0 & e^{f}_{32} \\ 0 & 0 & e^{f}_{33} \\ 0 & e^{f}_{24} & 0 \\ e^{f}_{15} & 0 & 0 \\ 0 & 0 & 0 \end{bmatrix} \begin{bmatrix} E^{f}_{1} \\ E^{f}_{2} \\ E^{f}_{3} \end{bmatrix}, \tag{4}$$

$$\begin{bmatrix} D^{f}_{1} \\ D^{f}_{2} \\ D^{f}_{3} \end{bmatrix} = \begin{bmatrix} 0 & 0 & 0 & 0 & e^{f}_{15} & 0 \\ 0 & 0 & 0 & e^{f}_{24} & 0 & 0 \\ e^{f}_{31} & e^{f}_{32} & e^{f}_{33} & 0 & 0 & 0 \end{bmatrix} \begin{bmatrix} s^{f}_{11} \\ s^{f}_{22} \\ s^{f}_{33} \\ 2s^{f}_{23} \\ 2s^{f}_{13} \\ 2s^{f}_{12} \end{bmatrix} + \begin{bmatrix} \varepsilon^{f}_{11} & 0 & 0 \\ 0 & \varepsilon^{f}_{22} & 0 \\ 0 & 0 & \varepsilon^{f}_{33} \end{bmatrix} \begin{bmatrix} E^{f}_{1} \\ E^{f}_{2} \\ E^{f}_{3} \end{bmatrix}, \tag{5}$$

where all constants are the complex constants of Eq. (2). The PZT-5A fibers are transversely isotropic about the poling axis x_3 (class $6mm$), so that

$$c^{f}_{22} = c^{f}_{11}, \quad c^{f}_{23} = c^{f}_{13}, \quad c^{f}_{55} = c^{f}_{44}, \quad c^{f}_{66} = \tfrac{1}{2}(c^{f}_{11} - c^{f}_{12}), \quad e^{f}_{32} = e^{f}_{31}, \quad e^{f}_{24} = e^{f}_{15}, \quad \varepsilon^{f}_{22} = \varepsilon^{f}_{11}, \tag{6}$$

and the same relations hold for the relaxation times. In particular, $e^{f}_{32} = e^{f}_{31} = -6.98$ C/m^2 is used in Appendix A.

The viscoelastic, piezoelectrically inert matrix obeys [5, 48]

$$\tau_I^q = c_{IJ}^q s_J^q, \qquad D_i^q = \varepsilon_{ij}^q E_j^q, \tag{7}$$

in Voigt notation, with the same structure of c_{IJ}^q as in Eq. (4) and $c_{22}^q = c_{11}^q$, $c_{23}^q = c_{13}^q$, $c_{55}^q = c_{44}^q$ (Table 1). The superscripts f and q refer to the fiber and matrix phases; τ_{ij}, s_{ij}, E_i and D_i denote stress, strain, electric field and electric displacement, respectively.

Following Guha and Singh [47], the VRFRC is represented by rectangular representative volume elements containing both constituents, with continuous, parallel and perfectly bonded fibers. The electric field is identical in both phases, $E_i^f = E_i^q = E_i$, and the longitudinal strain is common to both phases, $s_{11}^f = s_{11}^q = s_{11}$. The remaining strains, the stresses and the electric displacements follow from the rule of mixtures (RM) [47, 49]:

$$s_{ij} = V_f s_{ij}^f + V_q s_{ij}^q \ \ (ij \neq 11), \tag{8}$$

$$\tau_{11} = V_f \tau_{11}^f + V_q \tau_{11}^q, \qquad \tau_{ij} = \tau_{ij}^f = \tau_{ij}^q \ \ (ij \neq 11), \tag{9}$$

$$D_i = V_f D_i^f + V_q D_i^q, \tag{10}$$

where V_f and $V_q = 1 - V_f$ are the fiber and matrix volume fractions. The effective density is [50]

$$\rho = V_f \rho^f + V_q \rho^q. \tag{11}$$

Equations (8)–(10), together with the iso-strain and iso-field conditions, are linear algebraic relations between the phase fields. In the frequency domain the constitutive laws of the viscoelastic phases have exactly the form of the elastic ones with the real constants replaced by the complex constants of Eq. (2). By the elastic–viscoelastic correspondence principle, the effective complex constants of the VRFRC are therefore obtained by substituting the complex constituent constants of *both* phases into the closed-form SM/RM expressions given in Appendix A. Viscosity is thus introduced at the constituent level, before homogenization, and the effective constants

$$c_{ij} = c_{ij}(\omega), \qquad e_{ij} = e_{ij}(\omega), \qquad \varepsilon_{ij} = \varepsilon_{ij}(\omega) \tag{12}$$

are complex and frequency-dependent. The effective loss of a constant is not a volume-weighted value: for instance, $c_{44} = c_{44}^f c_{44}^q / (V_q c_{44}^f + V_f c_{44}^q)$ combines the fiber and matrix losses in series, and e_{15}, e_{31}, e_{33} are complex through the complex stiffnesses even though e_{ij}^f is real ($\eta_{ij}^{e,f} = 0$). The effective medium is transversely isotropic with the same symmetry as the constituents, so that $c_{55} = c_{44}$. The closed-form expressions of Appendix A were verified against a direct numerical solution of Eqs. (8)–(10) with complex constituent constants (maximum relative difference 1.8×10^{-14} for $V_f \in [0, 1]$ and $0 \leq f \leq 10$ MHz); they return exactly the matrix constants for $V_f = 0$ and the fiber constants for $V_f = 1$ for all eleven quantities c_{11}, c_{13}, c_{33}, c_{44}, c_{55}, e_{15}, e_{31}, e_{33}, ε_{11}, ε_{33} and ρ; and the passivity condition, Eq. (3), holds for the homogenized constants for all $V_f \in [0, 1]$ and 1 kHz $\leq f \leq$ 10 MHz (smallest eigenvalue of $\mathbf{L}$ non-negative to rounding). The computational procedure is summarized in Fig. 2.

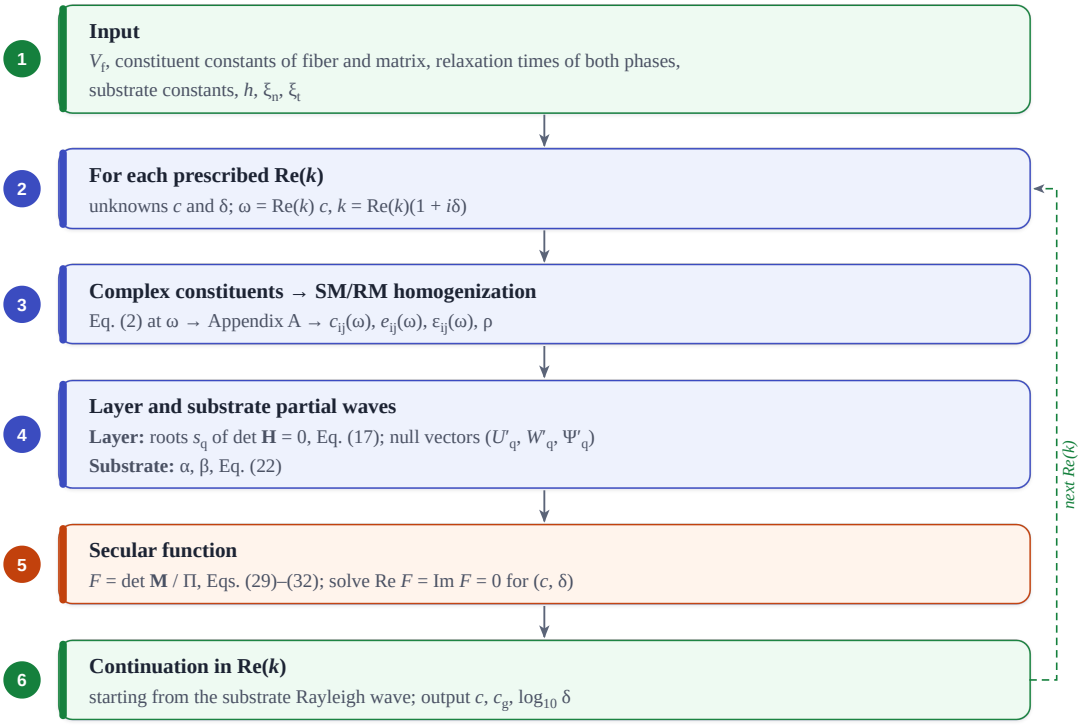


Fig. 2. Computational procedure for the dispersion and attenuation of Rayleigh-type waves in the VRFRC layer/elastic half-space system.

2.3. Solution for the VRFRC layer

For the transversely isotropic VRFRC layer with no body force or free charge, the relevant constitutive relations are

$$\left.\begin{aligned} \tau_{11} &= c_{11}\frac{\partial u}{\partial x} + c_{13}\frac{\partial w}{\partial z} + e_{31}\frac{\partial \phi}{\partial z}, & \tau_{33} &= c_{13}\frac{\partial u}{\partial x} + c_{33}\frac{\partial w}{\partial z} + e_{33}\frac{\partial \phi}{\partial z}, \\ \tau_{13} &= c_{44}\left(\frac{\partial u}{\partial z} + \frac{\partial w}{\partial x}\right) + e_{15}\frac{\partial \phi}{\partial x}, & & \\ D_1 &= e_{15}\left(\frac{\partial w}{\partial x} + \frac{\partial u}{\partial z}\right) - \varepsilon_{11}\frac{\partial \phi}{\partial x}, & D_3 &= e_{31}\frac{\partial u}{\partial x} + e_{33}\frac{\partial w}{\partial z} - \varepsilon_{33}\frac{\partial \phi}{\partial z}, \end{aligned}\right\} \tag{13}$$

which are Eqs. (4)–(5) for the homogenized medium with $E_i = -\partial\phi/\partial x_i$ and $c_{55} = c_{44}$. The equations of motion $\tau_{ij,j} = \rho\ddot{u}_i$ and Gauss' law $D_{i,i} = 0$ give

$$\begin{aligned} &c_{11}u_{,xx} + c_{44}u_{,zz} + (c_{13} + c_{44})w_{,xz} + (e_{31} + e_{15})\phi_{,xz} = \rho\ddot{u}, \\ &(c_{13} + c_{44})u_{,xz} + c_{44}w_{,xx} + c_{33}w_{,zz} + e_{15}\phi_{,xx} + e_{33}\phi_{,zz} = \rho\ddot{w}, \\ &(e_{15} + e_{31})u_{,xz} + e_{15}w_{,xx} + e_{33}w_{,zz} - \varepsilon_{11}\phi_{,xx} - \varepsilon_{33}\phi_{,zz} = 0. \end{aligned} \tag{14}$$

We seek solutions

$$(u, w, \phi) = (U, W, \varphi)\, e^{sz}\, e^{i(kx - \omega t)}, \qquad k = \mathrm{Re}(k) + i\,\mathrm{Im}(k) = \mathrm{Re}(k)\,(1 + i\delta)\,, \tag{15}$$

where ω is the real angular frequency, k the complex wavenumber, $c = \omega/\mathrm{Re}(k)$ the phase velocity and $\delta = \mathrm{Im}(k)/\mathrm{Re}(k)$ the normalized attenuation; for real k, $e^{i(kx-\omega t)} = e^{ik(x-ct)}$. Substitution into Eq. (14) gives

$$\mathbf{H}(s)\begin{bmatrix} U \\ W \\ \varphi \end{bmatrix} = \mathbf{0}, \qquad \mathbf{H}(s) = \begin{bmatrix} -c_{11}k^2 + c_{44}s^2 + \rho\omega^2 & iks(c_{13}+c_{44}) & iks(e_{31}+e_{15}) \\ iks(c_{13}+c_{44}) & -c_{44}k^2 + c_{33}s^2 + \rho\omega^2 & -e_{15}k^2 + e_{33}s^2 \\ iks(e_{15}+e_{31}) & -e_{15}k^2 + e_{33}s^2 & \varepsilon_{11}k^2 - \varepsilon_{33}s^2 \end{bmatrix}. \tag{16}$$

Dimensionally, the entries $H_{11}, H_{12}, H_{21}, H_{22}$ are a stiffness times k^2, the coupling entries $H_{13}, H_{23}, H_{31}, H_{32}$ a piezoelectric constant times k^2, and H_{33} a dielectric constant times k^2. Since k is complex, the inertia term is $\rho\omega^2 = \rho v^2 k^2$ with the complex velocity $v = \omega/k = c/(1+i\delta)$; it reduces to $\rho c^2 k^2$ only for $\delta = 0$. With $p = (s/k)^2$, $\det\mathbf{H} = k^6 D(p)$, and the condition $\det\mathbf{H} = 0$ is the cubic equation

$$D(p) \equiv a_3 p^3 + a_2 p^2 + a_1 p + a_0 = 0, \tag{17}$$

$$\begin{aligned}
a_3 &= -c_{44}(c_{33}\varepsilon_{33} + e_{33}^2), \\
a_2 &= c_{33}c_{44}\varepsilon_{11} + c_{33}(e_{31}+e_{15})^2 + \varepsilon_{33}[c_{44}B + c_{33}A - (c_{13}+c_{44})^2] + 2e_{33}[c_{44}e_{15} - (c_{13}+c_{44})(e_{31}+e_{15})] + e_{33}^2 A, \\
a_1 &= -\varepsilon_{33}AB - c_{44}e_{15}^2 - \varepsilon_{11}[c_{44}B + c_{33}A - (c_{13}+c_{44})^2] - 2e_{15}[e_{33}A - (c_{13}+c_{44})(e_{31}+e_{15})] - (e_{31}+e_{15})^2 B, \\
a_0 &= A(e_{15}^2 + \varepsilon_{11}B), \qquad A = c_{11} - \rho v^2, \qquad B = c_{44} - \rho v^2.
\end{aligned}$$

Each coefficient has the dimension (stiffness)^2×(dielectric constant) = (stiffness)×(piezoelectric constant)^2. These coefficients were checked against the symbolic expansion of $\det\mathbf{H}$ and numerically against the determinant for 200 random sets of complex constants (maximum relative difference 4.5×10^{-15}). The three roots p_m ($m = 1, 2, 3$) give six roots

$$s_q = \pm k\sqrt{p_m} \qquad (q = 1, \ldots, 6). \tag{18}$$

In the half-space problem only the three roots with $\mathrm{Re}(s_q) < 0$ are admissible; since the layer is finite, all six partial waves are retained:

$$(u^L, w^L, \phi^L) = \sum_{q=1}^{6} \left(U'_q, W'_q, \Psi'_q\right) \varphi_q \, e^{s_q z} \, e^{i(kx-\omega t)}, \tag{19}$$

where $\mathbf{r}_q = (U'_q, W'_q, \Psi'_q)^T$ is a null vector of $\mathbf{H}(s_q)$, normalized to $\|\mathbf{r}_q\| = 1$, and φ_q are unknown amplitudes. When $\Psi'_q \neq 0$ the null vector may be rescaled to $(U_q/\varphi_q, W_q/\varphi_q, 1)$.

Using Eqs. (13) and (19), the stresses and the electric displacement in the layer are

$$\begin{aligned}
\tau_{33}^L &= \sum_{q=1}^{6} (ik\, c_{13} U'_q + s_q\, c_{33} W'_q + s_q\, e_{33} \Psi'_q)\varphi_q \, e^{s_q z} e^{i(kx-\omega t)}, \\
\tau_{13}^L &= \sum_{q=1}^{6} (c_{44}(s_q U'_q + ikW'_q) + ik\, e_{15} \Psi'_q)\varphi_q \, e^{s_q z} e^{i(kx-\omega t)}, \\
D_3^L &= \sum_{q=1}^{6} (ik\, e_{31} U'_q + s_q\, e_{33} W'_q - s_q\, \varepsilon_{33} \Psi'_q)\varphi_q \, e^{s_q z} e^{i(kx-\omega t)}.
\end{aligned} \tag{20}$$

2.4. Elastic half-space

The isotropic elastic substrate ($z \geq h$) has Lamé constants λ_s, μ_s, density ρ_s and bulk velocities $c_L = \sqrt{(\lambda_s + 2\mu_s)/\rho_s}$, $c_T = \sqrt{\mu_s/\rho_s}$. The longitudinal and shear partial waves that decay with depth are

$$\begin{aligned} u^S &= \left[iB_1 e^{-k\alpha(z-h)} - \beta B_2 e^{-k\beta(z-h)}\right] e^{i(kx-\omega t)}, \\ w^S &= \left[-\alpha B_1 e^{-k\alpha(z-h)} - iB_2 e^{-k\beta(z-h)}\right] e^{i(kx-\omega t)}, \end{aligned} \tag{21}$$

$$\alpha = \sqrt{1 - v^2/c_L^2}, \qquad \beta = \sqrt{1 - v^2/c_T^2}, \qquad \mathrm{Re}(k\alpha) > 0, \;\; \mathrm{Re}(k\beta) > 0, \tag{22}$$

i.e. the branch of each square root is chosen such that the partial waves decay as $z \to \infty$. Substituting Eq. (21) into $\tau_{33} = \lambda_s(u_{,x} + w_{,z}) + 2\mu_s w_{,z}$ and $\tau_{13} = \mu_s(u_{,z} + w_{,x})$ and using $\lambda_s + 2\mu_s = \mu_s c_L^2/c_T^2$ gives the tractions

$$\begin{aligned} \tau_{33}^S &= k\mu_s \left[(1+\beta^2) B_1 e^{-k\alpha(z-h)} + 2i\beta B_2 e^{-k\beta(z-h)}\right] e^{i(kx-\omega t)}, \\ \tau_{13}^S &= k\mu_s \left[-2i\alpha B_1 e^{-k\alpha(z-h)} + (1+\beta^2) B_2 e^{-k\beta(z-h)}\right] e^{i(kx-\omega t)}. \end{aligned} \tag{23}$$

Because the substrate is a conductor, no electric field penetrates it.

3. Boundary and interface conditions

The upper surface is traction-free and electrically open:

$$\tau_{33}^L = \tau_{13}^L = 0, \qquad D_3^L = 0 \qquad \text{at } z = 0. \tag{24}$$

At $z = h$ the bond is imperfect. Following the linear-slip (spring) model [37–39], the tractions are continuous and proportional to the jumps of the corresponding displacements, and the grounded metallic substrate fixes the potential:

$$\tau_{33}^L = \tau_{33}^S, \quad \tau_{13}^L = \tau_{13}^S, \quad w^S - w^L = \frac{\tau_{33}}{K_n}, \quad u^S - u^L = \frac{\tau_{13}}{K_t}, \quad \phi^L = 0 \qquad \text{at } z = h, \tag{25}$$

where K_n and K_t (N/m^3) are the normal and tangential interfacial stiffnesses. Here τ_{33} and τ_{13} are the tractions that the substrate exerts on the lower face of the layer (outward normal $+z$). The springs transmit the forces $K_n(w^S - w^L)$ and $K_t(u^S - u^L)$ per unit area, so that a tensile stress $\tau_{33} > 0$ opens the interface ($w^S > w^L$, z pointing into the substrate) and $\tau_{13} > 0$ corresponds to $u^S > u^L$; the stored spring energy $\frac{1}{2}K_n|w^S - w^L|^2 + \frac{1}{2}K_t|u^S - u^L|^2$ is then non-negative for $K_n, K_t > 0$. We introduce the dimensionless interfacial compliances

$$\xi_n = \frac{\mu_s}{K_n h}, \qquad \xi_t = \frac{\mu_s}{K_t h}, \tag{26}$$

so that $\xi_n = \xi_t = 0$ corresponds to perfect bonding and $\xi_n, \xi_t \to \infty$ to a mechanically detached layer. The electrical condition $\phi^L = 0$ at $z = h$ is kept in both limits: even a mechanically detached layer remains electroded by the grounded substrate.

4. Secular Equation and Attenuation

Substituting Eqs. (19)–(23) into Eqs. (24)–(25) gives a homogeneous system of eight equations for the eight amplitudes $\mathbf{A} = (\varphi_1, \ldots, \varphi_6, B_1, B_2)^T$,

$$\mathbf{M}\,\mathbf{A} = \mathbf{0}. \tag{27}$$

With

$$M_{1q} = ik\,c_{13}U_q' + c_{33}s_qW_q' + e_{33}s_q\Psi_q', \quad M_{2q} = c_{44}(s_qU_q' + ikW_q') + ik\,e_{15}\Psi_q', \quad M_{3q} = ik\,e_{31}U_q' + e_{33}s_qW_q' - \varepsilon_{33}s_q\Psi_q', \tag{28}$$

($q = 1, \ldots, 6$), which reduce to the entries of the half-space problem for $\Psi_q' = 1$, and $E_q = e^{s_q h}$, the columns of the 8×8 matrix $\mathbf{M}$ are

$$\mathbf{M}_{\cdot q} = \begin{bmatrix} M_{1q} \\ M_{2q} \\ M_{3q} \\ M_{1q}E_q \\ M_{2q}E_q \\ -W_q'E_q - (\xi_n h/\mu_s)\,M_{1q}E_q \\ -U_q'E_q - (\xi_t h/\mu_s)\,M_{2q}E_q \\ \Psi_q'E_q \end{bmatrix} (q = 1, \ldots, 6), \quad \mathbf{M}_{\cdot 7} = \begin{bmatrix} 0 \\ 0 \\ 0 \\ -k\mu_s(1+\beta^2) \\ 2ik\mu_s\alpha \\ -\alpha \\ i \\ 0 \end{bmatrix}, \quad \mathbf{M}_{\cdot 8} = \begin{bmatrix} 0 \\ 0 \\ 0 \\ -2ik\mu_s\beta \\ -k\mu_s(1+\beta^2) \\ -i \\ -\beta \\ 0 \end{bmatrix}. \tag{29}$$

Rows 1–3 express Eq. (24); rows 4–5 the continuity of τ_{33} and τ_{13}; and row 8 the condition $\phi^L(h) = 0$. Rows 6–7 are obtained directly from the spring residuals of Eq. (25),

$$w^S(h) - w^L(h) - \frac{\xi_n h}{\mu_s}\,\tau_{33}^L(h) = 0, \qquad u^S(h) - u^L(h) - \frac{\xi_t h}{\mu_s}\,\tau_{13}^L(h) = 0, \tag{30}$$

with $1/K_{n,t} = \xi_{n,t}h/\mu_s$. A layer partial wave contributes $-W_q'E_q$ (from $-w^L$) and $-(\xi_n h/\mu_s)M_{1q}E_q$ (from $-\tau_{33}^L/K_n$) to row 6, and a substrate wave contributes its vertical displacement amplitude at $z = h$ ($-\alpha$ for B_1, $-i$ for B_2); row 7 is formed in the same way with U_q', M_{2q} and the horizontal amplitudes (i, $-\beta$). These are exactly the entries of Eq. (29), and the computer implementation uses the same signs. As an independent check, the fields were rebuilt from the null vector of $\mathbf{M}$ at computed roots ($V_f = 0.6$ with $(\xi_n, \xi_t) = (0.25, 0.25)$, $(1, 0)$, $(0, 1)$, and $V_f = 0.9$ with $(1, 1)$; $\mathrm{Re}(k) = 1200\ \mathrm{m}^{-1}$), and the tractions and D_3 were evaluated by numerical differentiation of the rebuilt fields instead of from the rows of $\mathbf{M}$. All eight conditions, Eqs. (24)–(25), are then satisfied with relative residuals below 2×10^{-11}, whereas the spring conditions with the opposite sign are violated by 8–98%. A displacement jump in w appears only for $\xi_n > 0$ and a jump in u only for $\xi_t > 0$ (e.g. $|w^S - w^L|/|w(0)| = 0.30$ and $|u^S - u^L| = 0$ for $\xi_n = 1$, $\xi_t = 0$). For non-trivial amplitudes,

$$\det \mathbf{M} = 0. \tag{31}$$

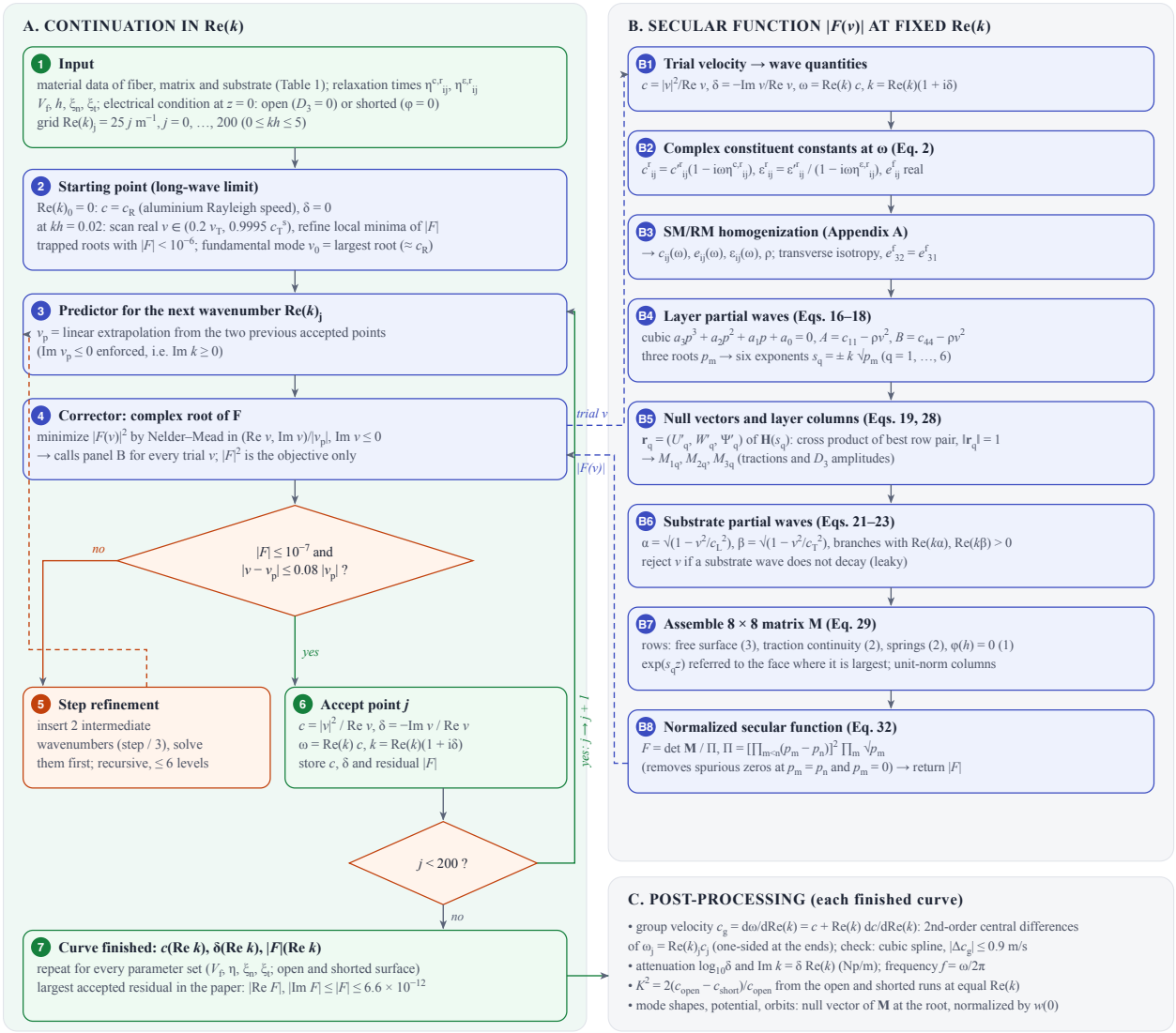


Fig. 3. Numerical algorithm for the dispersion, attenuation and group velocity of the fundamental mode

4.1. Numerical procedure

Here, $\det \mathbf{M}$ vanishes at the following values of v that are not dispersion roots: (i) If two roots of Eq. (17) coincide, $p_m = p_n$ $(m \neq n)$, the two partial waves $+k\sqrt{p_m}$, $+k\sqrt{p_n}$ and likewise the two partial waves $-k\sqrt{p_m}$, $-k\sqrt{p_n}$ become identical, so that $\mathbf{M}$ has two pairs of equal columns. Choosing locally an analytic normalization of the null vectors (e.g. one fixed non-vanishing component equal to 1; any other normalization multiplies a column by a non-zero factor), $\mathbf{r}_q$ and E_q are analytic functions of s_q, so that each pair of columns differs by $O(\sqrt{p_m} - \sqrt{p_n})$, and $\det \mathbf{M} = O((\sqrt{p_m} - \sqrt{p_n})^2) = O((p_m - p_n)^2)$. (ii) If $p_m = 0$, the two columns $\pm k\sqrt{p_m}$ coincide and $\det \mathbf{M} = O(\sqrt{p_m})$. These

zeros are removed by solving

$$F(c,\delta) \equiv \frac{\det \mathbf{M}}{\Pi} = 0, \qquad \Pi = \Big[\prod_{m<n}(p_m - p_n)\Big]^2 \prod_{m=1}^{3} \sqrt{p_m}. \tag{32}$$

Π is symmetric in the roots and therefore does not depend on their ordering; the sign of each $\sqrt{p_m}$ only changes the sign of F. Since $\Pi \neq 0$ except at the isolated coalescence points, the division never removes a zero of $\det \mathbf{M}$ elsewhere. If two coalescing partial waves have linearly independent null vectors, which is possible only when $\mathbf{H}$ decouples ($V_f = 0$), the columns do not coincide and F has an isolated pole instead of a removable zero; a pole can neither create nor hide a root of a continuous branch, and the $V_f = 0$ results below agree with an independent decoupled formulation. The removal was tested numerically (see Fig. 3). For $V_f = 0.3$ (elastic constants, $kh = 1$), two roots coalesce at $v_c = 434.177$ m/s. For $v = v_c(1+\epsilon)$, $\epsilon = 10^{-2}, \ldots, 10^{-5}$, both $|\det \mathbf{M}|$ and Π decrease in proportion to ϵ (since $p_m - p_n \propto \sqrt{\epsilon}$ near the branch point), while $|F|$ remains finite and non-zero ($|F| \approx 1.34 \times 10^{-6}$ in normalized units). The test was repeated at $kh = 3$ for the same material and for the lossy case $V_f = 0.9$, $kh = 1$ (complex coalescence point $v_c = 914.70 - 12.10\,i$ m/s), with the same behavior ($|F| = 4.08 \times 10^{-5}$ constant to three digits for $\epsilon = 10^{-2}, \ldots, 10^{-4}$). The zeros of $\det \mathbf{M}$ at these points are therefore spurious, and no physical root is lost.

For numerical stability each exponential is referred to the boundary at which it is largest ($e^{s_q z}$ for $\mathrm{Re}\, s_q \leq 0$ and $e^{s_q(z-h)}$ otherwise, i.e. the corresponding column is multiplied by the non-zero constant $e^{-s_q h}$), the columns of $\mathbf{M}$ are normalized to unit norm, and the stiffness, piezoelectric and dielectric constants are scaled by $c_0 = |c_{44}|$, $\sqrt{c_0 \varepsilon_0}$ and $\varepsilon_0 = |\varepsilon_{33}|$. Each of these operations multiplies $\det \mathbf{M}$ by a non-zero factor and leaves the roots unchanged; the same applies to any other normalization of the null vectors. The choice of the square-root branches of p_m does not affect the layer solution, because both $\pm k\sqrt{p_m}$ are retained; only α and β require the decay rule of Eq. (22).

Since the effective constants depend on $\omega = \mathrm{Re}(k)\, c$, Eq. (32) is a complex equation, i.e. the two real equations $\mathrm{Re}\, F = 0$ and $\mathrm{Im}\, F = 0$, for the two real unknowns c and δ at a prescribed $\mathrm{Re}(k)$. They are solved simultaneously, without the small-attenuation approximation: $|F|^2$ is minimized with a Nelder–Mead search in the complex v plane (with $\mathrm{Im}\, v \leq 0$, i.e. $\mathrm{Im}\, k \geq 0$), and $|F|^2$ is used only as the numerical objective. A point is accepted only if both residuals vanish, $|\mathrm{Re}\, F| \leq |F| \leq 10^{-7}$ and $|\mathrm{Im}\, F| \leq |F| \leq 10^{-7}$ in the normalized units (the residual $|F|$ stored for every accepted point bounds both); the largest residual of all accepted points in this paper is 6.6×10^{-12} and no accepted point has an exactly vanishing residual other than the analytic limit $\mathrm{Re}(k) = 0$. The fundamental branch is started at $kh = 0.02$ from the fastest trapped real root below the substrate shear speed, which coincides with the substrate Rayleigh wave, and is continued in $\mathrm{Re}(k)$ with a linear predictor extrapolated from the two previous points. Whenever the residual exceeds 10^{-7} or the corrected velocity differs from the predictor by more than 8%, the step is subdivided into three sub-steps (recursively, up to six levels), which prevents switching to another mode. The absence of branch switching was confirmed by repeating the curves with a second, independent implementation (different null-vector construction, different minimizer and different initial guesses): the two sets of curves agree to 9.6×10^{-13} in c and 8.1×10^{-8} in δ.

4.2. Attenuation

The attenuation is represented either by the dimensional spatial attenuation coefficient $\mathrm{Im}(k)$ (Np/m) or by the normalized attenuation $\delta = \mathrm{Im}(k)/\mathrm{Re}(k)$, plotted as $\log_{10}\delta$. Over one wavelength $\lambda = 2\pi/\mathrm{Re}(k)$ the amplitude decreases by the factor $e^{-2\pi\delta}$.

4.3. Group velocity

The group velocity of the real dispersion branch (the group velocity of the weakly damped wave) is

$$c_g = \frac{\mathrm{d}\omega}{\mathrm{d}\,(\mathrm{Re}(k))} = c + \mathrm{Re}(k)\,\frac{\mathrm{d}c}{\mathrm{d}\,(\mathrm{Re}(k))}, \tag{33}$$

evaluated with second-order central differences of $\omega = \mathrm{Re}(k)\,c$ on the computed grid ($\Delta\mathrm{Re}(k) = 25\ \mathrm{m}^{-1}$); a cubic-spline derivative gives the same values to within 0.9 m/s. c_g is the slope of the real dispersion branch; no energy-flux calculation is made, and c_g is not interpreted as an energy velocity, which in a dissipative medium may differ from it.

5. Validation and Special Cases

The formulation simplifies to numerous classical issues, which were utilized to test the numerical implementation (Fig. 4):

- **Long-wave limit** ($kh \to 0$): the fundamental mode tends to the Rayleigh wave of the aluminium substrate, $c_R = 2921.19$ m/s (Fig. 4(a)).
- **Short-wave limit** ($kh \to \infty$): the wave is confined to the layer and tends to the Rayleigh-type surface wave of a VRFRC half-space with an electrically open surface [51]. Computed at $kh = 60$ with elastic constants, the limiting speeds are 1019.44, 1042.66 and 1486.13 m/s for $V_f = 0.3$, 0.6 and 0.9 (dotted lines in Fig. 4(a)).
- **Volume-fraction limits** (complete dispersion problem): for $V_f = 0$ the layer is the epoxy matrix, a non-piezoelectric transversely isotropic solid, and $\mathbf{H}$ decouples (Sec. 2.3). Because general unit null vectors are used, the unified 8×8 formulation remains well defined; its dispersion curves coincide with those of an independently assembled, purely elastic 6×6 formulation (four mechanical partial waves and two substrate waves) to a relative difference below 5×10^{-12} for $\xi_n = \xi_t = 0$ and 1, and they are continuous as $V_f \to 0^+$ (e.g. $c = 2315.9$, 2319.6 and 2346.7 m/s at $\mathrm{Re}(k) = 1000\ \mathrm{m}^{-1}$ for $V_f = 0$, 10^{-3} and 10^{-2}). The short-wave limit for $V_f = 0$, 918.592 m/s, agrees with the closed-form Rayleigh speed of the orthotropic epoxy half-space, 918.592 m/s. For $V_f = 1$ the layer is the PZT fiber material and the short-wave limit is 2276.49 m/s. Both limits start from c_R at $kh \to 0$.
- **Homogeneous half-space**: when the layer has the properties of the substrate and $\xi_n = \xi_t = 0$, $c = c_R$ for every kh; the computed velocity agrees with the exact Rayleigh speed to a relative error below 10^{-13}.
- **Detached layer** ($\xi_n, \xi_t \to \infty$): mechanically, the layer becomes a free plate whose fundamental mode is the antisymmetric Lamb mode A_0 [52]. For an isotropic, non-piezoelectric epoxy layer, for which the grounded lower face has no mechanical influence, the estimated velocities with $\xi_n = \xi_t = 10^{14}$ coincide with the precise A_0 velocities to a relative difference below 8.1×10^{-8} (Fig. 4(b)). For a piezoelectric layer the detached limit is a free plate that is electroded on its lower face.
- **Elastic fibers in a viscoelastic matrix**: $\eta_{ij}^{c,f} = \eta_{ij}^{e,f} = \eta_{ij}^{e,f} = 0$ recovers the description in which only the matrix is dissipative (Fig. 13).

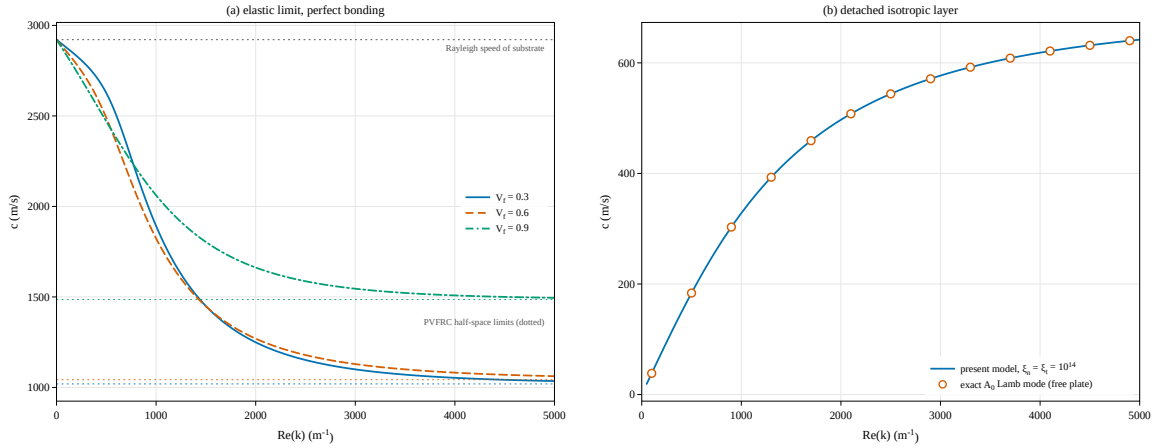


Fig. 4. Validation. (a) Elastic limit with perfect bonding: phase velocity of the fundamental mode for $V_f = 0.3, 0.6, 0.9$; the gray dotted line is the Rayleigh speed of the substrate ($kh \to 0$) and the lower dotted lines are the Rayleigh speeds of the corresponding VRFRC half-spaces ($kh \to \infty$). (b) Detached isotropic layer ($\xi_n = \xi_t = 10^{14}$): present model compared with the exact A_0 Lamb mode of a free plate.

6. Numerical Results and Discussion

The material data are used for the formulation of VPFRC medium is listed in Table 1. For aluminium ($\lambda_s = 58.5$ GPa, $\mu_s = 26.4$ GPa, $\rho_s = 2700$ kg/m^3), $c_L = 6420.45$ m/s, $c_T = 3126.94$ m/s, and the Rayleigh equation $(2 - v^2/c_T^2)^2 = 4\alpha\beta$ provides $c_R = 2921.19$ m/s. The substrate is aluminium, the layer thickness is $h = 1$ mm, and the wavenumber range $0 \le \mathrm{Re}(k) \le 5000$ m^{-1} ($0 \le kh \le 5$) corresponds to frequencies up to roughly 1.2 MHz. The base relaxation times are $\eta_{ij}^{c,q} = \eta_{ij}^{\varepsilon,q} = 10$ ns for the epoxy matrix and $\eta_{ij}^{c,f} = \eta_{ij}^{\varepsilon,f} = 1$ ns for the PZT fibers, with $\eta_{ij}^{e,f} = 0$. The relaxation times are material constants, whereas the loss tangents $\omega\eta$ expand with frequency: at 500 kHz they are 0.031 (matrix) and 0.0031 (fibers), and at 1 MHz 0.063 and 0.0063, values characteristic of epoxy and of piezoceramics in this frequency range. Unless specified otherwise the interface is great. Table 2 lists the effective constants at 500 kHz, computed from Appendix A with the data of Table 1 and $e_{32}^f = e_{31}^f$; every entry was recreated by an independent implementation of Appendix A.

Table 1. Material data used in the computations. The fiber and matrix constants are the storage (primed) values of Eq. (2); the remaining constants follow from Eq. (6).

Constant	PZT-5A fiber	Epoxy matrix	Aluminium substrate
$c_{11} = c_{22}$, c_{12}, $c_{13} = c_{23}$ (GPa)	139, 77.8, 75.4	3.86, 2.57, 2.57	$\lambda_s = 58.5$
c_{33}, $c_{44} = c_{55}$ (GPa)	113, 25.6	3.86, 2.57	$\mu_s = 26.4$
$e_{15} = e_{24}$, $e_{31} = e_{32}$, e_{33} (C/m^2)	13.4, −6.98, 13.8	0, 0, 0	–
$\varepsilon_{11} = \varepsilon_{22}$, ε_{33} (10^{-9} F/m)	6.00, 5.47	0.079, 0.079	conductor
ρ (kg/m^3)	7750	1210	2700
η_{ij}^c, η_{ij}^ε (ns), base values	1, 1	10, 10	–

Table 2. Effective constants of the VRFRC at $f = 500$ kHz for $V_f = 0.3, 0.6, 0.9$: elastic constituents, base relaxation times ($\eta^q = 10$ ns, $\eta^f = 1$ ns) and increased matrix relaxation times ($\eta^q = 20$ ns, $\eta^f = 1$ ns). η^q and η^f denote $\eta^c_{ij} = \eta^e_{ij}$ of the matrix and of the fibers; $\eta^{e,f}_{ij} = 0$ and $e^f_{32} = e^f_{31}$.

	Elastic			$\eta^q = 10$ ns, $\eta^f = 1$ ns			$\eta^q = 20$ ns, $\eta^f = 1$ ns		
Constant	$V_f = 0.3$	$V_f = 0.6$	$V_f = 0.9$	$V_f = 0.3$	$V_f = 0.6$	$V_f = 0.9$	$V_f = 0.3$	$V_f = 0.6$	$V_f = 0.9$
ρ (kg/m^3)	3172	5134	7096	3172	5134	7096	3172	5134	7096
c_{11} (GPa)	28.15	53.52	87.25	$28.15 - 0.203\,i$	$53.52 - 0.315\,i$	$87.26 - 0.605\,i$	$28.15 - 0.331\,i$	$53.52 - 0.478\,i$	$87.26 - 0.972\,i$
c_{13} (GPa)	3.620	6.118	19.69	$3.620 - 0.112\,i$	$6.118 - 0.184\,i$	$19.69 - 0.488\,i$	$3.620 - 0.224\,i$	$6.119 - 0.367\,i$	$19.70 - 0.960\,i$
c_{33} (GPa)	5.435	9.180	29.52	$5.435 - 0.169\,i$	$9.180 - 0.276\,i$	$29.53 - 0.731\,i$	$5.435 - 0.337\,i$	$9.181 - 0.550\,i$	$29.54 - 1.44\,i$
c_{44} (GPa)	3.520	5.584	13.50	$3.520 - 0.106\,i$	$5.585 - 0.155\,i$	$13.50 - 0.243\,i$	$3.520 - 0.212\,i$	$5.586 - 0.307\,i$	$13.51 - 0.465\,i$
e_{15} (C/m^2)	0.5527	1.754	6.360	$0.5528 - 0.0150\,i$	$1.754 - 0.0431\,i$	$6.362 - 0.0944\,i$	$0.5529 - 0.0316\,i$	$1.755 - 0.0910\,i$	$6.367 - 0.199\,i$
e_{31} (C/m^2)	−3.280	−6.450	−8.810	$-3.280 - 0.0020\,i$	$-6.450 - 0.0067\,i$	$-8.810 - 0.0254\,i$	$-3.280 - 0.0042\,i$	$-6.449 - 0.0142\,i$	$-8.809 - 0.0536\,i$
e_{33} (C/m^2)	0.1995	0.6740	3.251	$0.1996 - 0.0056\,i$	$0.6741 - 0.0181\,i$	$3.251 - 0.0703\,i$	$0.1996 - 0.0117\,i$	$0.6743 - 0.0383\,i$	$3.253 - 0.148\,i$
ε_{11} (10^{-9} F/m)	3.873	7.289	8.724	$3.873 + 0.0161\,i$	$7.289 + 0.0373\,i$	$8.723 + 0.0721\,i$	$3.872 + 0.0204\,i$	$7.289 + 0.0533\,i$	$8.721 + 0.122\,i$
ε_{33} (10^{-9} F/m)	3.072	5.986	8.273	$3.072 + 0.0117\,i$	$5.986 + 0.0227\,i$	$8.273 + 0.0450\,i$	$3.072 + 0.0139\,i$	$5.986 + 0.0271\,i$	$8.272 + 0.0661\,i$

Table 3. Passivity check of every relaxation-time set used in the figures: smallest eigenvalue of the complete 9×9 loss matrix of the matrix and fiber constituents (normalized by the constituent c_{44} and ε_{33}, $f = 1$ MHz) and of the 5×5 loss matrix of the homogenized medium (minimum over $V_f \in [0, 1]$ and 10 kHz $\le f \le$ 1.5 MHz). Unless stated, $\eta^q = 10$ ns and $\eta^f = 1$ ns. The last row is the case $\eta^{c,q}_{13} = 20$ ns, which is *not* used.

Relaxation-time set	Matrix	Fiber	Homogenized
Base	1.58×10^{-2}	6.28×10^{-3}	6.25×10^{-5}
$\eta^{c,q}_{11} = 15$, 20 ns	3.15×10^{-2}	6.28×10^{-3}	6.25×10^{-5}
$\eta^{c,q}_{33} = 15$, 20 ns	1.58×10^{-2}	6.28×10^{-3}	6.25×10^{-5}
$\eta^{c,q}_{44} = 15$, 20 ns	1.58×10^{-2}	6.28×10^{-3}	6.25×10^{-5}
$\eta^{c,q}_{13} = 5$ ns	1.58×10^{-2}	6.28×10^{-3}	6.25×10^{-5}
$\eta^{c,q}_{13} = 15$ ns	1.22×10^{-4}	6.28×10^{-3}	1.22×10^{-6}
$\eta^f = 0$ (elastic fibers)	1.58×10^{-2}	0	0
$\eta^f = 3$ ns	1.58×10^{-2}	1.88×10^{-2}	1.87×10^{-4}
$\eta^q = 15$ ns (uniform)	2.37×10^{-2}	6.28×10^{-3}	6.26×10^{-5}
$\eta^q = 20$ ns (uniform)	3.15×10^{-2}	6.28×10^{-3}	6.27×10^{-5}
$\eta^{c,q}_{13} = 20$ ns (not admissible)	-3.13×10^{-2}	6.28×10^{-3}	-4.67×10^{-2}

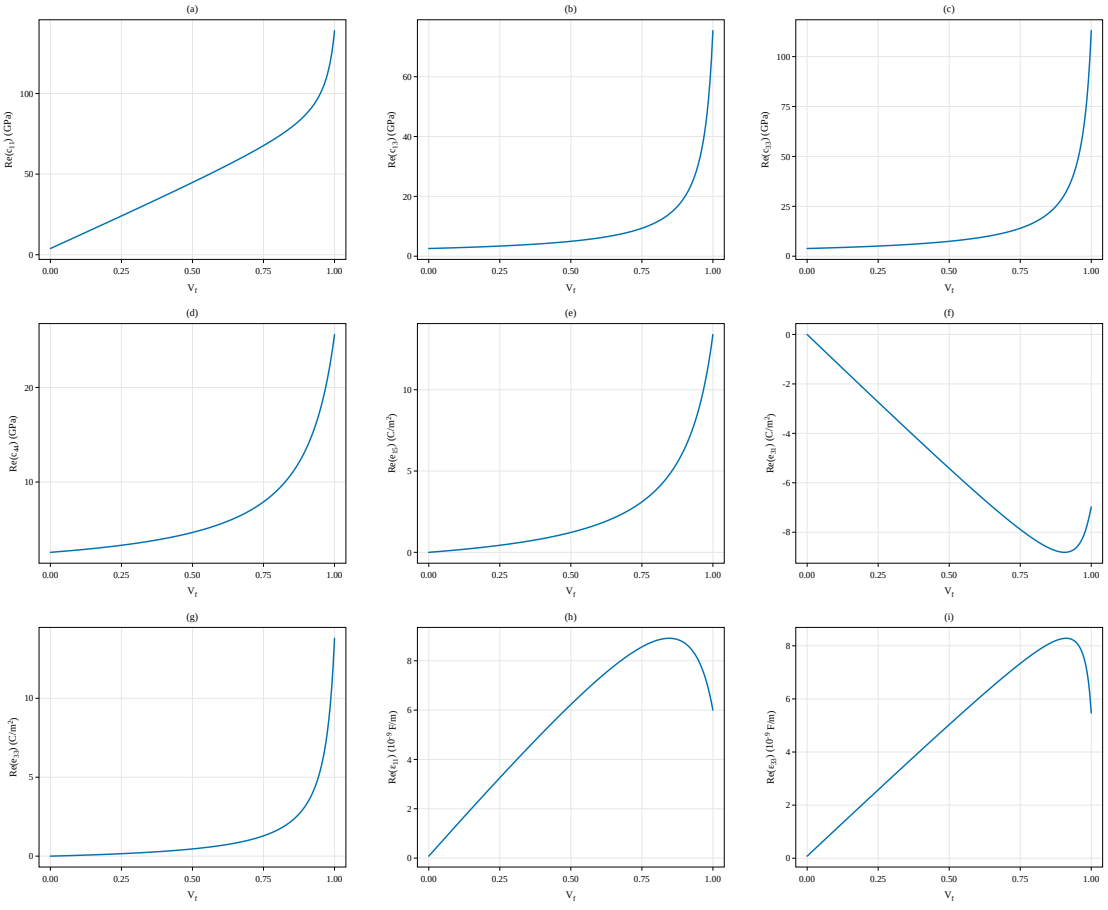


Fig. 5. Real (storage) parts of the effective constants of the VRFRC versus fiber volume fraction at $f = 500$ kHz: (a)–(d) c_{11}, c_{13}, c_{33}, c_{44}; (e)–(g) e_{15}, e_{31}, e_{33}; (h)–(i) ε_{11}, ε_{33} (base relaxation times; the storage parts are practically independent of the relaxation times).

6.1. *Effective properties*

Figs. 5–7 illustrate the real and imaginary portions of all effective constants vs V_f at 500 kHz. The storage sections (Fig. 5) are nearly independent of the relaxation times and rise with V_f. $\mathrm{Re}(c_{11})$ grows almost linearly, since it is governed by the iso-strain (parallel) coupling along the fibers, whereas $\mathrm{Re}(c_{13})$, $\mathrm{Re}(c_{33})$, $\mathrm{Re}(c_{44})$, $\mathrm{Re}(e_{15})$ and $\mathrm{Re}(e_{33})$ remain small up to $V_f \approx 0.8$ and then rise steeply, because they are governed by the series (iso-stress) coupling with the compliant matrix. $|\mathrm{Re}(e_{31})|$ attains its largest value (8.81 C/m^2) near $V_f \approx 0.91$, exceeding the fiber value $|e^f_{31}| = 6.98$ C/m^2; this enhancement arises from the transverse coupling terms γ_3, γ_6 of Appendix A (which contain e^f_{32} and e^f_{33}) and is a known feature of the SM/RM model. The permittivities reach their maxima at $V_f \approx 0.85$ (ε_{11}) and $V_f \approx 0.91$ (ε_{33}).

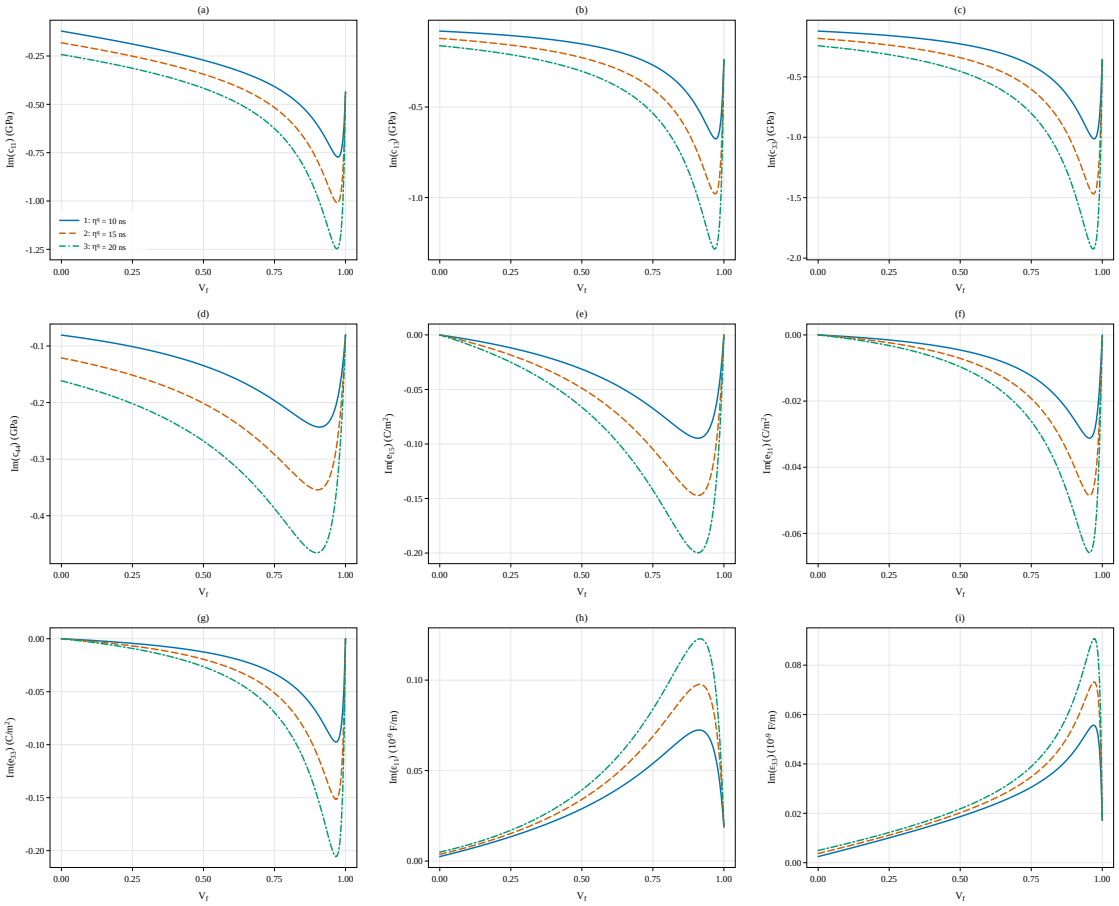


Fig. 6. Imaginary (loss) parts of the effective constants versus fiber volume fraction at $f = 500$ kHz for matrix relaxation times $\eta^q = 10$, 15 and 20 ns ($\eta^f = 1$ ns). Panels as in Fig. 5.

The imaginary components (Fig. 6) scale with the matrix relaxation time and are negative for the stiffness and piezoelectric constants and positive for the permittivities, as required for a passive material with time dependence $e^{-i\omega t}$. Their magnitudes expand with V_f and peak at high fiber content ($V_f \approx 0.91$–0.97), where the stiff fibers support the load while the deformation is concentrated in thin, lossy matrix ligaments; they decline abruptly as $V_f \to 1$ because the fibers are an order of magnitude less lossy. The loss factors (Fig. 7) indicate the dilution of the matrix loss

more clearly. For c_{33}, c_{13} and c_{44} the loss factor stays close to the matrix value $\omega\eta^q = 0.031$ up to $V_f \approx 0.8$ (series coupling; e.g. 0.028 for c_{33} and 0.023 for c_{44} at $V_f = 0.8$), whereas for c_{11} it falls to 0.009 already at $V_f = 0.2$ and to ≈ 0.006 at intermediate V_f, i.e. close to the fiber value (parallel coupling). All loss factors tend to the fiber value 0.0031 at $V_f = 1$. The dielectric loss factors are low (≈ 0.004–0.009) over most of the range because the permittivity is dominated by the low-loss fibers.

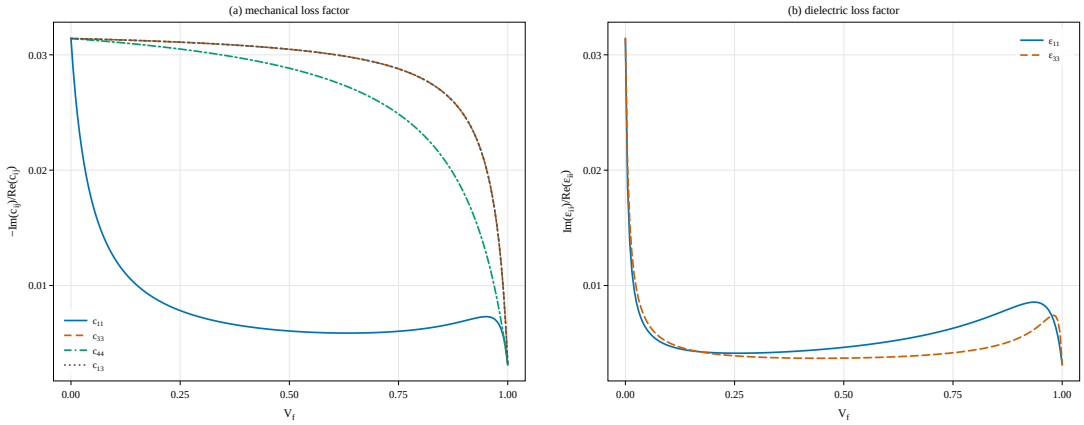


Fig. 7. Effective loss factors versus fiber volume fraction at $f = 500$ kHz (base relaxation times): (a) mechanical, $-\mathrm{Im}(c_{ij})/\mathrm{Re}(c_{ij})$ (the curves for c_{13} and c_{33} almost coincide); (b) dielectric, $\mathrm{Im}(\varepsilon_{ii})/\mathrm{Re}(\varepsilon_{ii})$.

6.2. *Effect of the fiber volume fraction*

Fig. 8 displays the dispersion and attenuation of the fundamental mode for the base parameters. All curves start at the substrate Rayleigh speed at $\mathrm{Re}(k) = 0$ and decline monotonically towards the surface-wave speed of the VRFRC half-space, since the motion (Fig. 17) migrates from the fast aluminium substrate into the slow composite layer as the wavelength lowers. The velocity drop is sharpest for $\mathrm{Re}(k) \approx 500$–$1500$ m^{-1}. At $\mathrm{Re}(k) = 1000$ m^{-1} the phase velocities are 1892.3, 1823.7 and 2061.5 m/s and at 5000 m^{-1} they are 1036.1, 1063.2 and 1497.2 m/s for $V_f = 0.3$, 0.6 and 0.9, near to their half-space limits. The higher stiffness and the stronger piezoelectric stiffening of the $V_f = 0.9$ layer retain its velocity much higher over most of the range. The attenuation is low in the long-wave region, where the motion is carried by the lossless substrate, and rises dramatically once the wave enters the lossy layer. In the dispersive range the attenuation reduces with increasing fiber content ($\log_{10}\delta = -1.69$, -1.90 and -2.45 at $\mathrm{Re}(k) = 1000$ m^{-1}), since the stiffer fiber-rich layer stores more energy per unit of matrix loss. At short wavelengths the three curves merge ($\log_{10}\delta \approx -1.62$ at 5000 m^{-1}), and for $V_f = 0.3$ a mild maximum appears near $\mathrm{Re}(k) \approx 1200$ m^{-1}, where the shear deformation of the soft layer is largest. The group velocity, Fig. 8(b), decreases significantly more steeply than the phase velocity and passes through a notable minimum: $c_g^{\min} = 549$, 682 and 1232 m/s at $\mathrm{Re}(k) \approx 1225$, 1300 and 1600 m^{-1} for $V_f = 0.3$, 0.6 and 0.9. It then recovers towards the phase velocity at short wavelengths ($c_g = 981$, 1001 and 1462 m/s at 5000 m^{-1}). Increasing the fiber content boosts the group velocity minimum and shifts it to greater wavenumbers. The minimum of c_g lies near to the maximum (or the end of the sharp increase) of the attenuation, i.e. the slope of the dispersion branch is smallest where the wave shifts from a substrate-dominated to a layer-dominated motion.

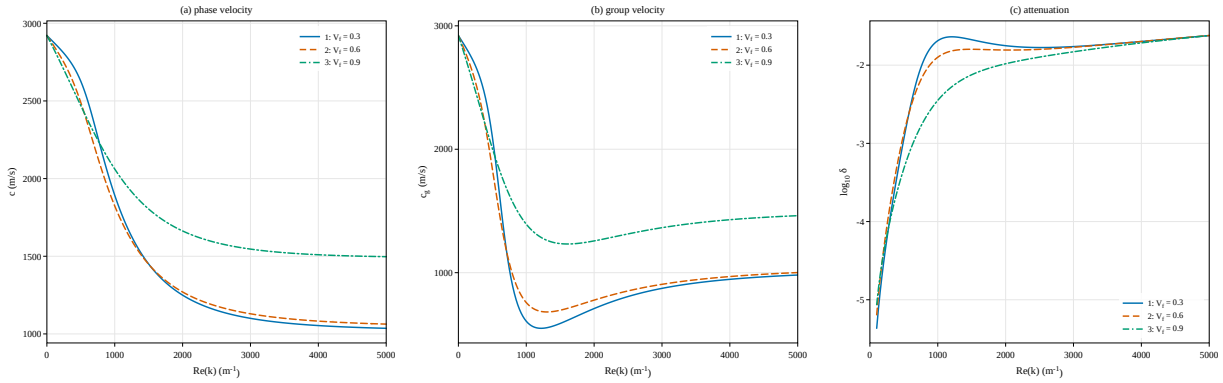


Fig. 8. Effect of the fiber volume fraction on (a) the phase velocity, (b) the group velocity and (c) the attenuation of the fundamental mode (perfect interface, base relaxation times).

6.3. Effect of the viscous relaxation times of the matrix

Figs. 9–12 demonstrate the influence of the matrix relaxation times $\eta_{11}^{c,q}$, $\eta_{33}^{c,q}$, $\eta_{44}^{c,q}$ and $\eta_{13}^{c,q}$, each varied independently with all other relaxation times at their base values (10 ns). $\eta_{11}^{c,q}$, $\eta_{33}^{c,q}$ and $\eta_{44}^{c,q}$ are varied from 10 to 20 ns; raising a diagonal entry of $[c'_{IJ}\eta^c_{IJ}]$ adds a positive semi-definite matrix and therefore preserves passivity. The off-diagonal relaxation time $\eta_{13}^{c,q}$ can only be modified within the permissible range $0 \leq \eta_{13}^{c,q} \leq 15.02$ ns (Sec. 2.2); it is therefore varied from 5 to 15 ns. The smallest eigenvalues of the constituent and effective loss matrices for every case are listed in Table 3; all cases are passive. In all cases the phase velocity remains practically unaltered (relative changes $< 0.4\%$), as expected for modest losses, where the velocity correction is of second order in $\omega\eta$, although the attenuation changes substantially. Increasing $\eta_{11}^{c,q}$ has essentially little effect (Fig. 9; $\Delta \log_{10}\delta \leq 0.007$): c_{11} is regulated by the stiff fibers in the iso-strain direction, thus the matrix loss in this constant is diluted. Increasing $\eta_{33}^{c,q}$ (Fig. 10) produces the biggest rise of attenuation in the dispersive range; for $V_f = 0.6$, $\log_{10}\delta$ at $\mathrm{Re}(k) = 1000$ m^{-1} increases from -1.90 to -1.75 and -1.64 for $\eta_{33}^{c,q} = 10$, 15 and 20 ns. Increasing $\eta_{44}^{c,q}$ (Fig. 11) mainly raises the attenuation at short wavelengths, where shear deformation of the layer dominates; for $V_f = 0.6$, $\log_{10}\delta$ at 5000 m^{-1} increases from -1.62 to -1.47 and -1.36, together with a slight increase of the phase velocity (from 1063.2 to 1065.9 m/s). In contrast, increasing $\eta_{13}^{c,q}$ (Fig. 12) slightly *reduces* the attenuation (e.g. $\log_{10}\delta$ at 1000 m^{-1} from -1.894 to -1.898 and -1.903 for $V_f = 0.6$, and from -1.678 to -1.687 and -1.696 for $V_f = 0.3$, for $\eta_{13}^{c,q} = 5$, 10 and 15 ns). The loss of c_{13} enters the dissipated power through the product of the normal strains s_{11} and s_{33}, which have opposite signs in the Rayleigh-type motion (Poisson effect), so that this contribution is negative and partly offsets the losses associated with c_{11} and c_{33}. Within the permissible range the overall dissipation density stays non-negative for every strain state (Table 3); above 15.02 ns the matrix would become active, which is why greater values of $\eta_{13}^{c,q}$ are not considered. The sensitivity to the matrix relaxation times is strongest at $V_f = 0.3$ and 0.6, where the matrix bears a higher share of the deformation, and is smaller but still noticeable at $V_f = 0.9$. The group velocity (middle rows of Figs. 9–12) is, like the phase velocity, practically insensitive to the matrix relaxation times: its minimum varies by less than 0.5% in all situations. The highest change occurs for $\eta_{44}^{c,q}$ at short wavelengths, where c_g at $\mathrm{Re}(k) = 5000$ m^{-1} increases from 1000.9 to 1004.4 and 1009.2 m/s for $V_f = 0.6$ (from 1461.8 to 1479.1 m/s for $V_f = 0.9$). In the dispersive range, the greater $\eta_{33}^{c,q}$ lowers $c_g^{\min}$ somewhat for $V_f = 0.3$ (from 549.3 to 546.8 m/s). Viscous relaxation in the matrix therefore influences the decay of the wave but scarcely impacts its group velocity.

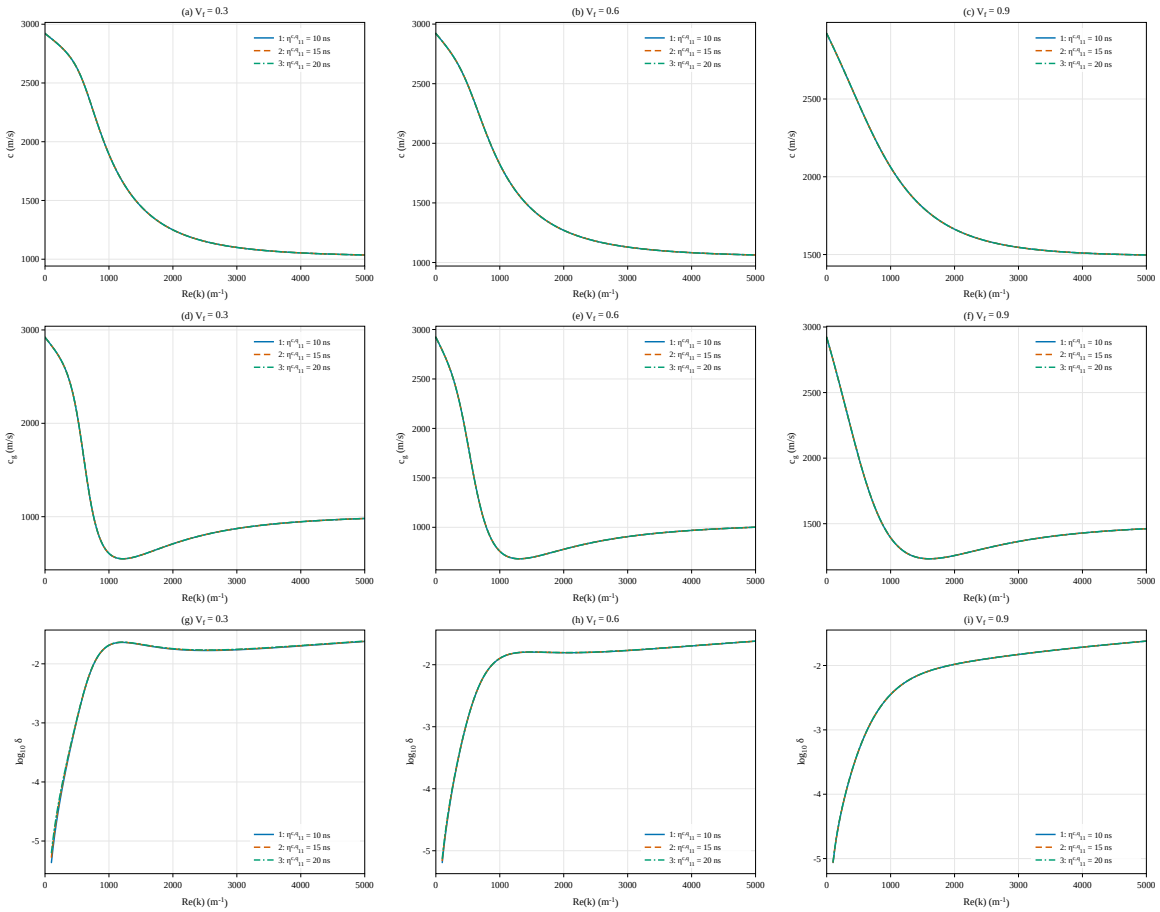


Fig. 9. Effect of $\eta_{11}^{c,q}$ on (a)–(c) the phase velocity, (d)–(f) the group velocity and (g)–(i) the attenuation for V_f = 0.3, 0.6, 0.9.

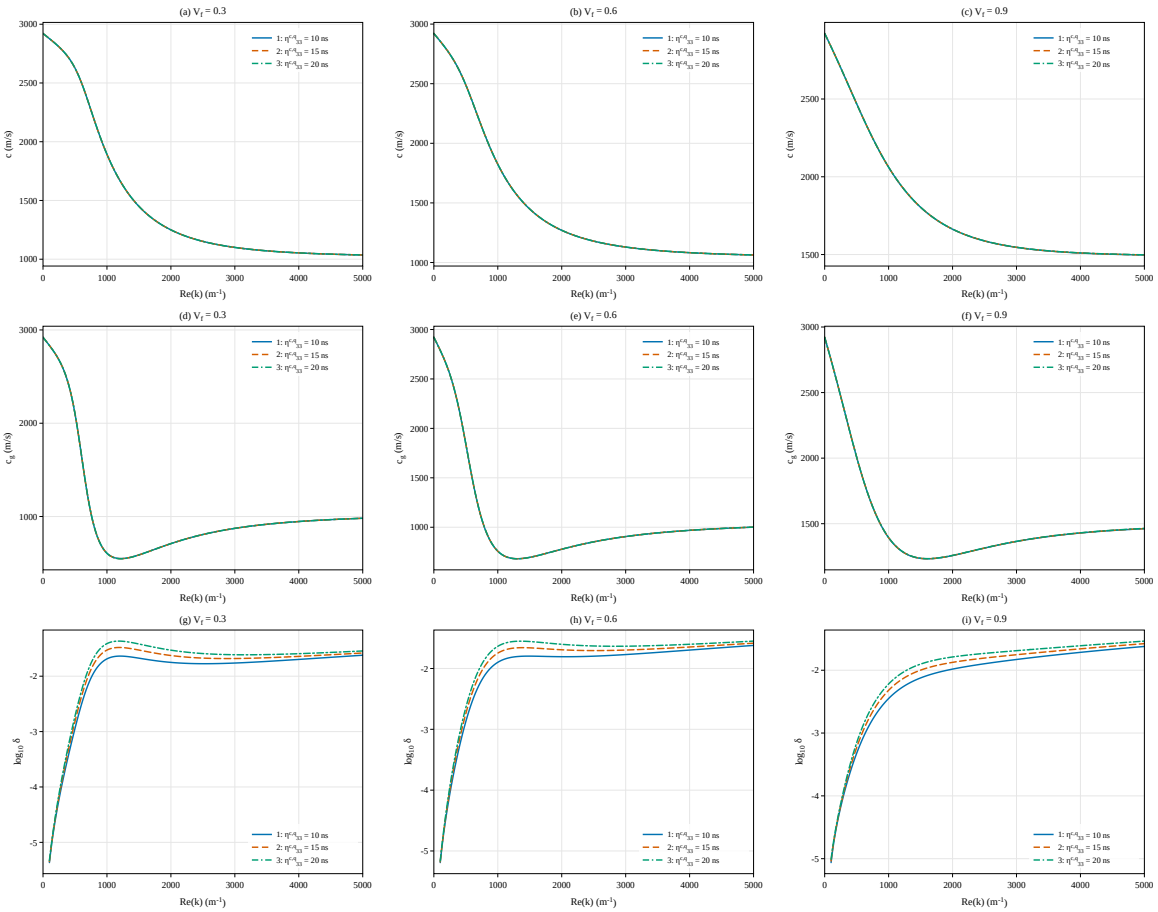


Fig. 10. Effect of $\eta_{33}^{c,q}$ on (a)–(c) the phase velocity, (d)–(f) the group velocity and (g)–(i) the attenuation for V_f = 0.3, 0.6, 0.9.

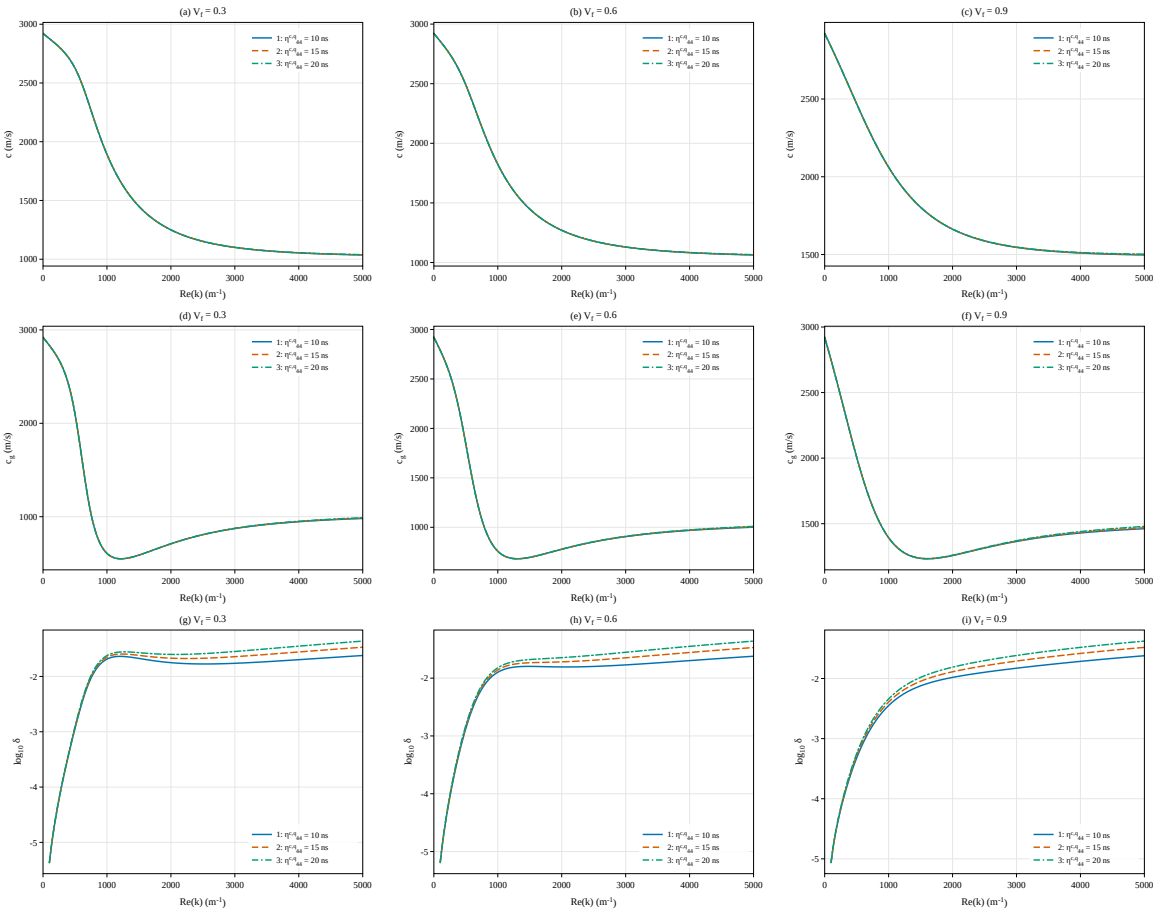


Fig. 11. Effect of $\eta_{44}^{c,q}$ on (a)–(c) the phase velocity, (d)–(f) the group velocity and (g)–(i) the attenuation for V_f = 0.3, 0.6, 0.9.

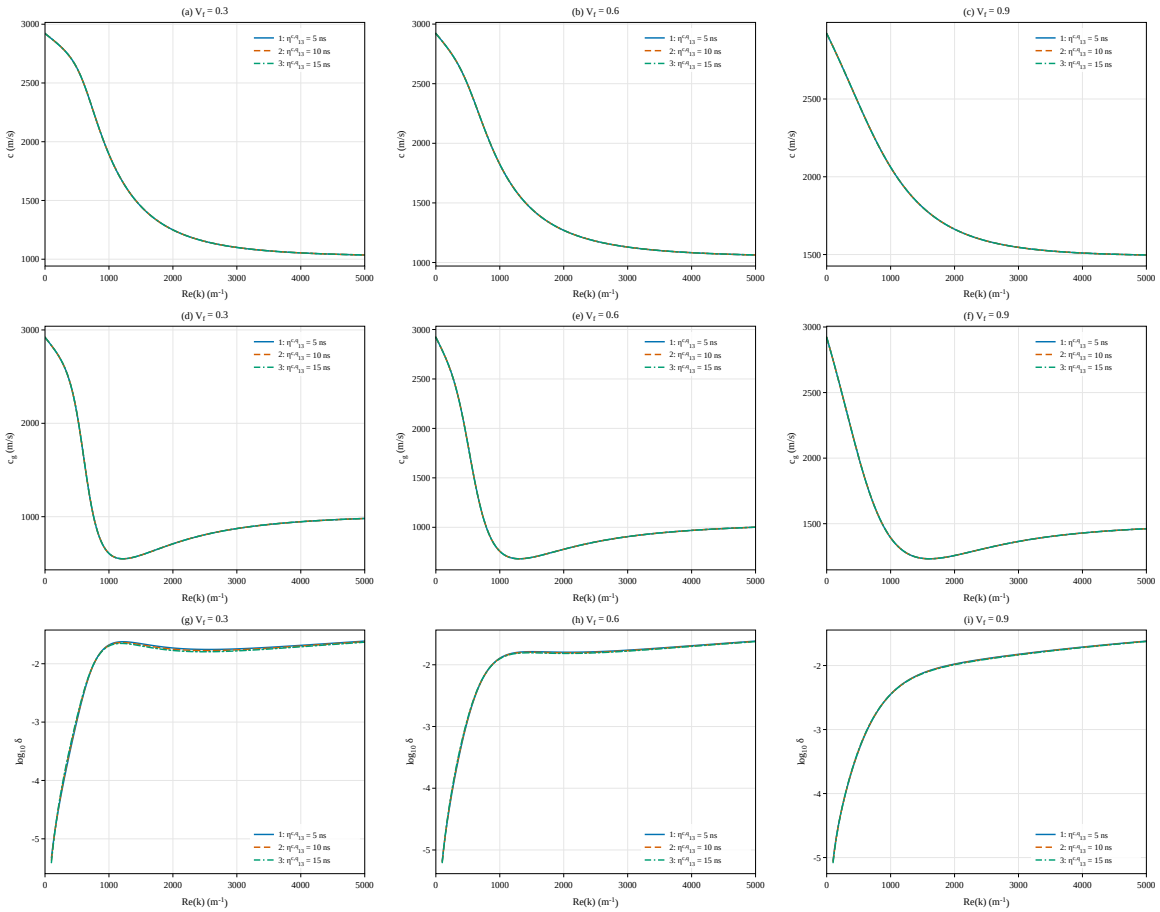


Fig. 12. Effect of $\eta^{c,q}_{13}$ (5, 10 and 15 ns, within the passive range $\eta^{c,q}_{13} \leq 15.02$ ns) on (a)–(c) the phase velocity, (d)–(f) the group velocity and (g)–(i) the attenuation for $V_f = 0.3, 0.6, 0.9$.

6.4. Effect of fiber viscoelasticity

Fig. 13 contrasts elastic fibers ($\eta^f = 0$) with viscoelastic fibers ($\eta^f = 1$ and 3 ns), keeping the matrix at its base values. The phase velocity is unaltered. For $V_f = 0.3$ and 0.6 the fiber loss changes the attenuation just significantly ($\Delta \log_{10}\delta \leq 0.02$ at 1000 m^{-1}), since the deformation is focused in the matrix. For $V_f = 0.9$ the effect is plainly visible: $\log_{10}\delta$ at Re(k) = 1000 m^{-1} increases from −2.48 (elastic fibers) to −2.45 and −2.40, and at 5000 m^{-1} from −1.65 to −1.62 and −1.57; the increase persists over the complete wavenumber range. Neglecting the viscoelasticity of the fibers therefore underestimates the attenuation of fiber-rich VRFRC layers, which warrants treating both phases as viscoelastic. The group velocity is unaffected by the fiber losses to within 0.2 m/s.

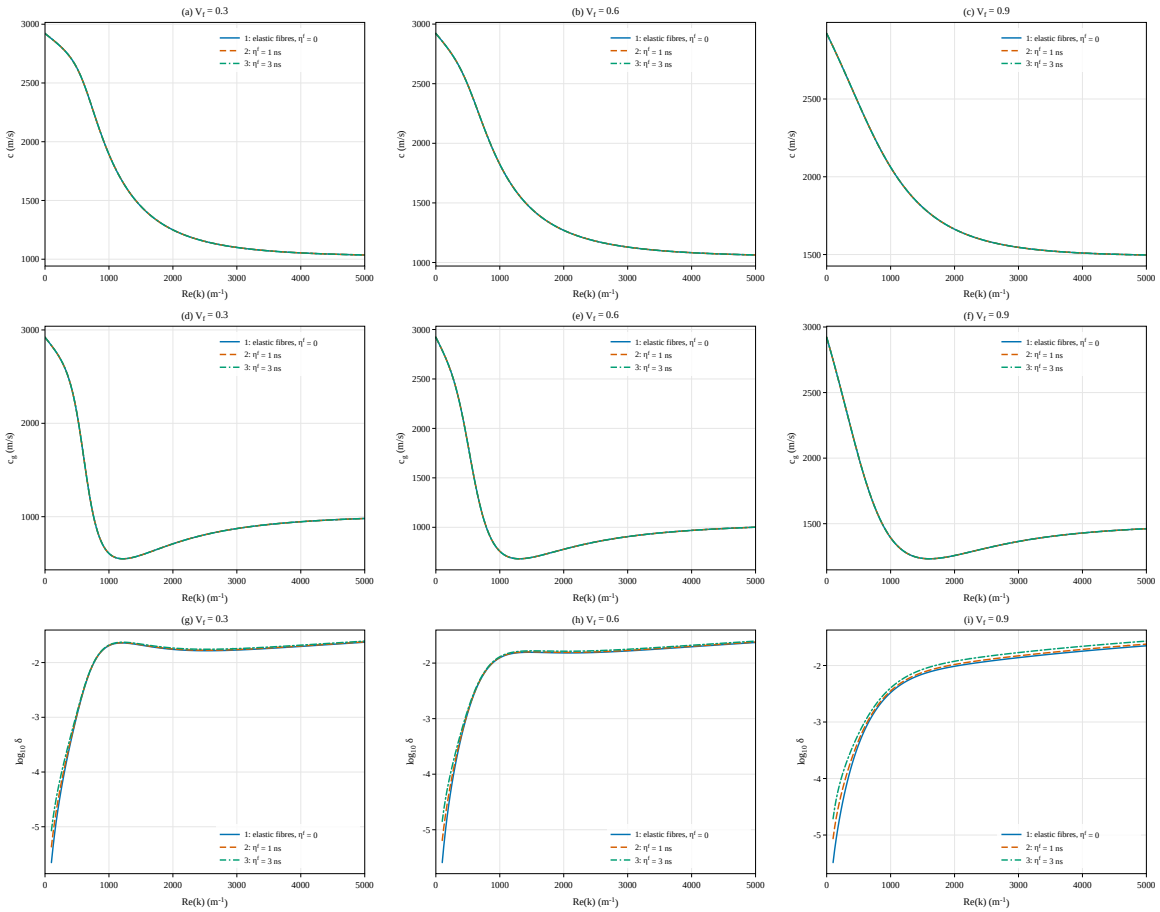


Fig. 13. Effect of the fiber relaxation time $\eta^f = \eta_{ij}^{c,f} = \eta_{ij}^{\varepsilon,f}$ on (a)–(c) the phase velocity, (d)–(f) the group velocity and (g)–(i) the attenuation for $V_f = 0.3, 0.6, 0.9$.

6.5. Effect of the imperfect interface

Fig. 14 demonstrates the effect of equal normal and tangential compliances $\xi_n = \xi_t \in \{0, 0.25, 1\}$. The interfacial compliance lowers the phase velocity throughout the dispersive range because it weakens the restriction that the stiff substrate exerts on the layer; for $V_f = 0.6$ and $\mathrm{Re}(k) = 1000$ m^{-1}, c decreases from 1823.7 m/s (ideal bond) to 1738.8 and 1544.3 m/s. The long-wave limit (substrate Rayleigh wave) is unaffected, and at $V_f = 0.3$ and 0.6 the curves approach the half-space limit again at short wavelengths, where the wave is localized near the free surface and senses the interface less. For $V_f = 0.9$ and $\xi = 1$ the phase velocity passes through a minimum ($c \approx 1394$ m/s near $\mathrm{Re}(k) \approx 2150$ m^{-1}) that lies below the surface-wave speed of the VRFRC half-space (1486 m/s), and then increases slowly towards it (1455.6 m/s at 5000 m^{-1}); a much weaker minimum (1481.6 m/s near 4250 m^{-1}) occurs for $\xi = 0.25$. In this regime the poorly bonded stiff layer behaves like a plate on a flexible basis and its flexural feature delays the wave. The attenuation in the dispersive range reduces with increasing compliance (e.g. $\log_{10}\delta$ at 1000 m^{-1} from -1.90 to -1.95 and -2.10 for $V_f = 0.6$), since a larger part of the deformation is taken up by the lossless interfacial springs instead of the viscoelastic layer. The group velocity (Fig. 14(d)–(f)) is impacted even more substantially than the phase velocity. Its minimum is dropped and moved to smaller wavenumbers: for $V_f = 0.6$, $c_g^{\min}$ declines from

682 m/s at Re(k) $\approx$ 1300 m^{-1} (perfect bond) to 676 m/s at 1200 m^{-1} ($\xi = 0.25$) and 635 m/s at 950 m^{-1} ($\xi = 1$). For $V_f = 0.9$ it reduces from 1232 m/s to 1146 m/s (1200 m^{-1}) and 918 m/s (850 m^{-1}). Beyond the minimum, c_g of the compliantly bonded layer climbs above that of the perfectly bonded one. Where the phase velocity increases with wavenumber (dc/dRe(k) > 0), Eq. (33) gives $c_g > c$ (anomalous dispersion); this occurs for $V_f = 0.9$ with $\xi = 1$ for Re(k) $\gtrsim$ 2175 m^{-1} (e.g. $c_g = 1533$ m/s > $c = 1456$ m/s at 5000 m^{-1}) and with $\xi = 0.25$ for Re(k) $\gtrsim$ 4250 m^{-1}.

Fig. 15 isolates the two compliances for $V_f = 0.6$. The normal compliance has by far the greatest influence: $\xi_n = 1$ alone lowers c at Re(k) = 1000 m^{-1} from 1823.7 to 1580.5 m/s, whereas $\xi_t = 1$ alone gives 1783.7 m/s, and the combined case (1544.3 m/s) is close to the purely normal one. This reflects the largely vertical motion of the fundamental mode in the dispersive range. The group velocity and the attenuation follow the same ordering: the minimum of c_g is 681.7 m/s (perfect), 679.3 m/s ($\xi_t = 1$), 670.6 m/s ($\xi_n = 1$) and 634.6 m/s ($\xi_n = \xi_t = 1$), and it moves from Re(k) $\approx$ 1300 to 1225, 1000 and 950 m^{-1}, respectively; $\log_{10}\delta$ at 1000 m^{-1} is −1.90, −1.94, −2.07 and −2.10.

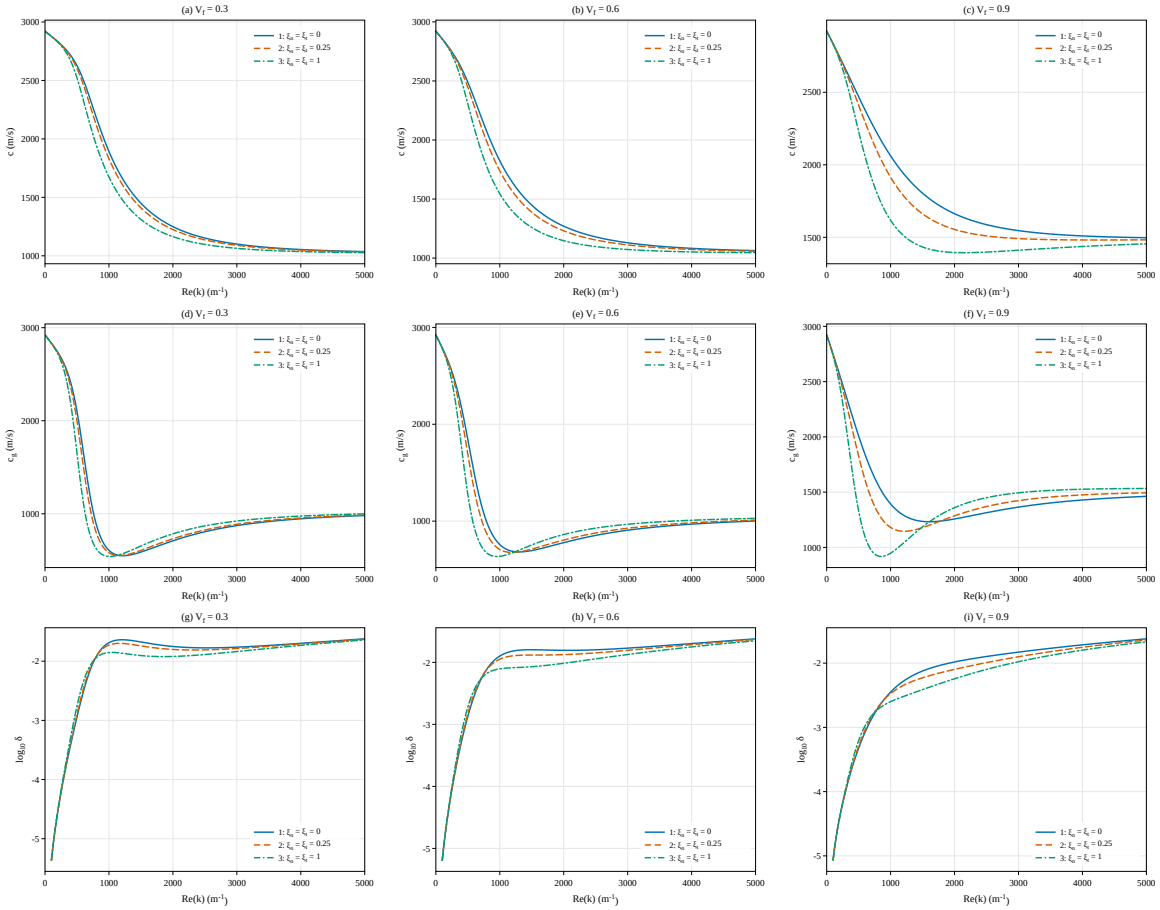


Fig. 14. Effect of the interfacial compliance $\xi_n = \xi_t$ on (a)–(c) the phase velocity, (d)–(f) the group velocity and (g)–(i) the attenuation for $V_f = 0.3$, 0.6, 0.9 (base relaxation times).

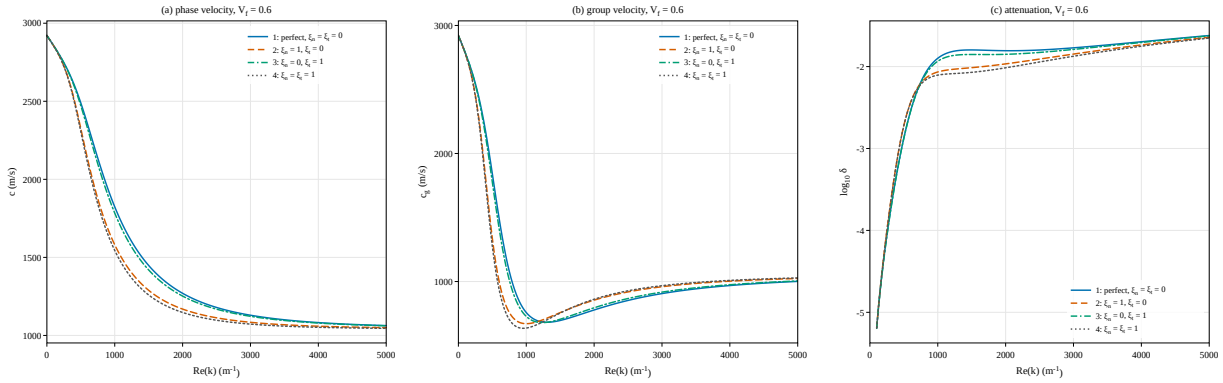


Fig. 15. Separate effects of the normal (ξ_n) and tangential (ξ_t) interfacial compliances on (a) the phase velocity, (b) the group velocity and (c) the attenuation for $V_f = 0.6$.

Fig. 16 follows the fundamental mode constantly in the interfacial compliance for fixed wavenumbers ($kh = 1$ and 3). The response has a sigmoidal form. For $\xi \lesssim 0.1$ the bond acts as perfect, the primary transition happens for $0.3 \lesssim \xi \lesssim 10$, and for $\xi \gtrsim 30$ the velocity approaches the flexural (A_0-type) mode of the detached VRFRC plate. For $V_f = 0.6$ and $kh = 1$, c declines from 1823 m/s ($\xi = 10^{-3}$) to 1544 m/s at $\xi = 1$ and to 721 m/s at $\xi = 100$. The attenuation decreases monotonically with ξ (by about one order of magnitude at $kh = 1$, e.g. $\log_{10}\delta$ from -1.90 to -2.92 for $V_f = 0.6$), and the sensitivity is much larger at $kh = 1$ than at $kh = 3$, where the wave is already confined near the free surface (for $V_f = 0.6$, c changes from 1130 to 953 m/s). This trend shows that phase-velocity measurements at intermediate kh are most suited to the non-destructive assessment of the bond quality.

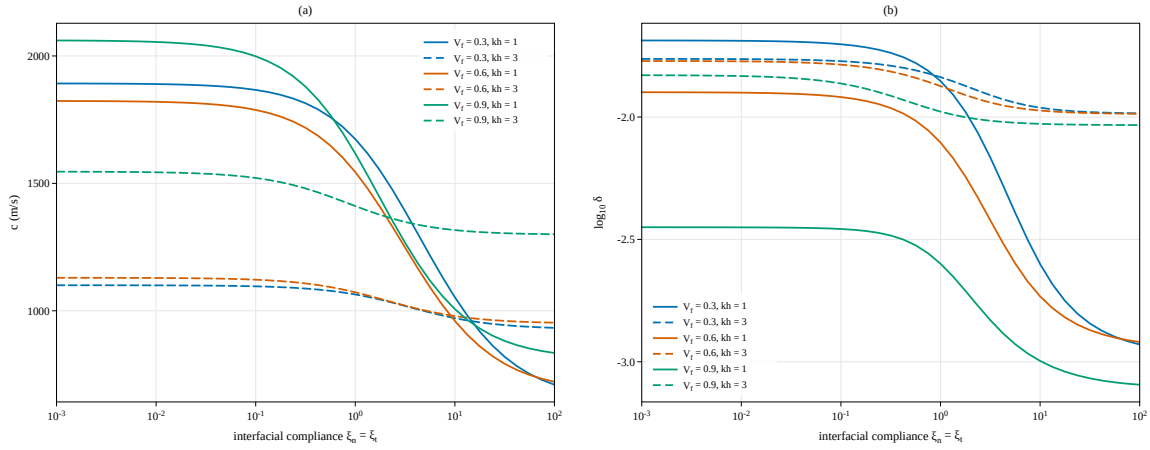


Fig. 16. (a) Phase velocity and (b) attenuation of the fundamental mode versus interfacial compliance $\xi_n = \xi_t$ at $kh = 1$ (solid) and $kh = 3$ (dashed), obtained by continuation in ξ.

6.6. Group velocity and frequency-domain characteristics

In addition to the group velocities given with each parametric study above, Fig. **??** compares the phase and group velocities, Eq. (33), directly. For the perfectly bonded layer the phase velocity decreases monotonically with Re(k) (normal dispersion) over the computed range, so that $c_g c$ occurs for the compliant interface (see above and Fig. **??**(f)).

The group velocity has a pronounced minimum (Airy phase), $c_g^{\min} = 549$, 682 and 1232 m/s at $\mathrm{Re}(k) \approx 1225$, 1300 and 1600 m^{-1} for $V_f = 0.3$, 0.6 and 0.9, located where the phase velocity decreases most rapidly with wavenumber, i.e. where the motion changes from substrate-dominated to layer-dominated. At short wavelengths c_g approaches c from below for the perfect bond ($c_g = 981$, 1001 and 1462 m/s at 5000 m^{-1}). Interfacial compliance pushes the minimum to smaller wavenumbers and lowers it, most dramatically for the stiff layer: for $V_f = 0.9$, $c_g^{\min}$ decreases from 1232 m/s (ideal bond) to 1146 and 918 m/s for $\xi = 0.25$ and 1. Because the damping is weak ($\delta \lesssim 0.03$), the group velocity of the real branch is a helpful kinematic indicator of narrow-band wave-packet arrival timings, and it is sensitive to both the fiber content and the bond quality.

6.7. Mode shapes, electric potential and particle motion

Fig. 17 displays the amplitudes of the horizontal and vertical displacements vs depth for $V_f = 0.6$, reconstructed from the null vector of $\mathbf{M}$ and normalized by $w(0)$. At $kh = 0.5$ the motion penetrates deep into the substrate (Rayleigh-wave nature of the substrate). At $kh = 1.5$ it is concentrated in the layer, and at $kh = 4$ it is essentially restricted to the layer, which explains the convergence of c to the half-space value. The horizontal displacement contains a node inside the layer ($z/h = 0.30$ for $kh = 1.5$), which marks the change of the perception of particle motion. For the imperfect interface ($\xi_n = \xi_t = 1$) both displacement components jump at $z = h$ according to Eq. (25). The leap in w is the larger one, consistent with the main role of the normal compliance, and the substrate motion is correspondingly reduced.

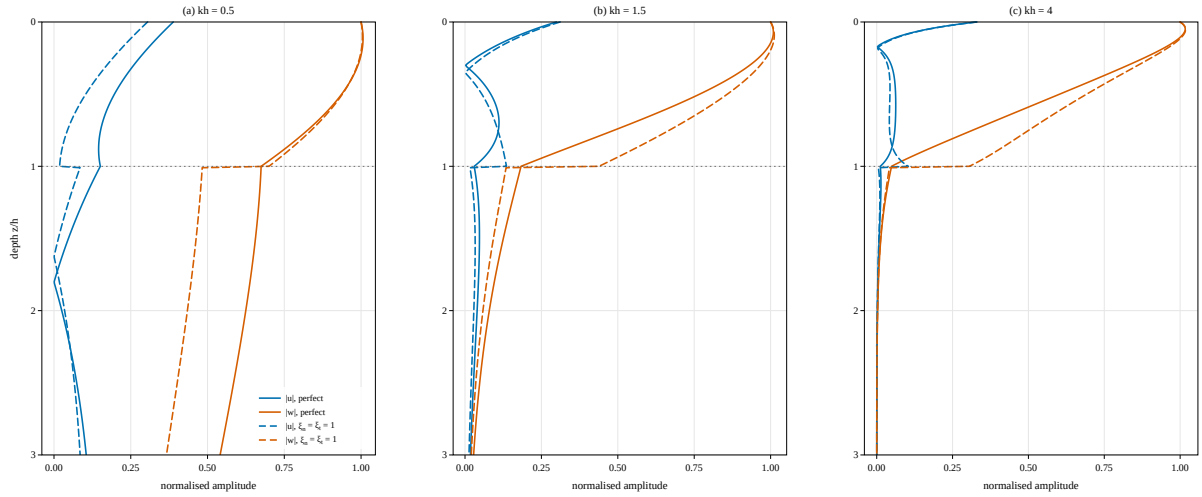


Fig. 17. Amplitudes of the horizontal ($|u|$) and vertical ($|w|$) displacements versus depth for $V_f = 0.6$ and $kh = 0.5, 1.5, 4$, perfect bond (solid) and $\xi_n = \xi_t = 1$ (dashed); normalized by $w(0)$.

7. Conclusions

Rayleigh-type wave propagation in a VRFRC layer inadequately attached to an isotropic elastic half-space has been investigated with both composite constituents treated as viscoelastic. The key conclusions are:

(i) Introducing passive Kelvin–Voigt-type complex constants in both phases and homogenizing them exactly through the SM/RM relations provides complex, frequency-dependent effective constants whose losses are not simple

volume averages. The dielectric loss must fulfill $\mathrm{Im}\,\varepsilon > 0$ (for $e^{-i\omega t}$); the form $\varepsilon' - i\omega\varepsilon''$ characterizes an active medium.

(ii) The exact 8×8 complex dispersion relation, solved for the phase velocity and attenuation without a small-loss approximation, reproduces the substrate Rayleigh wave ($kh \to 0$), the VRFRC half-space surface wave ($kh \to \infty$, including the closed-form epoxy limit $V_f = 0$), the classical Rayleigh wave for identical media, and the A_0 Lamb mode for a detached layer.

(iii) The fiber volume fraction governs the dispersion: a higher V_f enhances the phase velocity at short wavelengths and the group-velocity minimum, through larger layer stiffness and piezoelectric stiffening, and lowers the attenuation in the dispersive range.

(iv) The viscous relaxation durations of the matrix govern the attenuation but rarely affect the phase and group velocities (changes below 1.2%). $\eta_{33}^{c,q}$ dominates in the dispersive range and $\eta_{44}^{c,q}$ at short wavelengths, $\eta_{11}^{c,q}$ is completely useless, and $\eta_{13}^{c,q}$ somewhat reduces the attenuation. Independent relaxation times are not inherently admissible: with the other matrix relaxation times at 10 ns, passivity requires $\eta_{13}^{c,q} \leq 15.02$ ns.

(v) Fiber viscoelasticity is minimal at low fiber content but enhances the attenuation of fiber-rich layers ($V_f = 0.9$) substantially and should not be ignored.

(vi) Interfacial compliance, principally the normal compliance, lowers the phase velocity and the attenuation in the dispersive range; for stiff, weakly bonded layers it can cause a velocity minimum below the half-space surface-wave speed, beyond which $c_g > c$. The primary transition occurs for $0.3 \lesssim \xi \lesssim 10$, beyond which the mode approaches the flexural mode of the detached layer.

(vii) The group velocity exhibits a distinct minimum (Airy phase) whose value and position depend on V_f and on the bond quality, which makes it a sensitive indicator for non-destructive examination.

These results provide guidelines for the design and non-destructive assessment of bonded piezoelectric composite layers in structural health monitoring, ultrasonic sensing and vibration control.

Data Availability Statement

The datasets, analytical models and computational codes underlying the results of this study are available from the corresponding author upon reasonable request.

Acknowledgments

Mr. Bikram Dholey gratefully acknowledges the Council of Scientific and Industrial Research (CSIR), Human Resource Development Group (HRDG), Government of India, for the award of a Junior Research Fellowship (JRF) (File No. 09/0096(23009)/2025-EMR-I), which provided essential financial support for the present research.

Dr. Amrita Das sincerely acknowledges the financial support received from the Anusandhan National Research Foundation (ANRF), Department of Science and Technology (DST), Government of India, under Project No. EEQ/2022/000596, which significantly contributed to the successful completion of this work.

Conflict of Interest

The authors report that there are no conflicts of interest to declare.

References

[1] R. F. Gibson, A review of recent research on mechanics of multifunctional composite materials and structures, Composite structures 92 (2010) 2793–2810.

[2] S. Guha, A. K. Singh, Influence of varying fiber volume fractions on plane waves reflecting from the stress-free/rigid surface of a piezoelectric fiber-reinforced composite half-space, Mechanics of Advanced Materials and Structures 29 (2022) 5758–5772.

[3] M. Biswas, S. Guha, Influence of dynamic fiber volume fraction on love wave velocity in PFRC plate imperfectly bonded with piezoelectric-viscoelastic substrate, Acta Mechanica 236 (2025) 321–341.

[4] B. Dholey, K. C. Mistri, G. C. Shit, A. Das, Analysis of cylindrical membrane effects on shear-horizontal wave propagation in pfrc core–shell structures, Mathematical Methods in the Applied Sciences (2026) 1–22. doi:https://doi.org/10.1002/mma.70496.

[5] B. Dholey, K. C. Mistri, G. C. Shit, A. Das, Influence of interfacial stiffness and density on love-type wave propagation in a fiber-reinforced and fiber-piezoelectric layered medium, International Journal of Applied Mechanics (2026). doi:10.1142/S1758825126500080.

[6] J. Gao, D. Zheng, C. Tang, X. Gao, J. Fu, Y. Li, C. Li, M. Li, H. Wen, X. Li, et al., Accurate magnetic field estimation in fiber-coupled nanodiamond nv ensembles using model-assisted regression, Optics Express 34 (2026) 10040–10055.

[7] D. Gao, K. Zhang, C. Ding, D. Fang, Analytical model for pullout behavior of novel multiple hooked-end steel fiber in cementitious matrix, Mechanics of Materials (2026) 105652.

[8] K. C. Mistri, B. Dholey, S. K. Vishwakarma, A. Das, Influence of dual electric membranes pairing with a sandwiched electrically induced spring interface on SH-Wave propagation in smart porous composite, Journal of Vibration Engineering & Technologies 14 (2026) 176.

[9] K. Zheng, C. Huang, Research on the interfacial reinforcement mechanism and tribological performance of resin matrix composites reinforced with alumina sol-modified coconut shell fibers, Tribology International (2026) 112580.

[10] Y. He, Y. Jiang, Q. Li, M. Yuan, R. Fang, J. Lv, H. Zhang, H. He, Y. Wang, Detection and analysis of mechanical stress waves in igbts using a fiber-optic ring acoustic emission sensor, IEEE Transactions on Instrumentation and Measurement (2026).

[11] Y. Chen, Z. Guo, X.-L. Gao, L. Dong, Z. Zhong, Constitutive modeling of viscoelastic fiber-reinforced composites at finite deformations, Mechanics of Materials 131 (2019) 102–112. doi:https://doi.org/10.1016/j.mechmat.2019.02.001.

[12] A. K. Singh, K. C. Mistri, A. Das, Propagation of sh-wave in a corrugated viscous sandy layer sandwiched between two elastic half-spaces, Waves in Random and Complex Media 27 (2017) 213–240. doi:10.1080/17455030.2016.1213461.

[13] R. Holland, Representation of dielectric, elastic, and piezoelectric losses by complex coefficients, IEEE Transactions on Sonics and Ultrasonics 14 (1967) 18–20.

[14] A. K. Verma, A. Chattopadhyay, M. S. Chaki, A. K. Singh, Rayleigh-type wave propagation on a transversely isotropic viscoelastic layer with yielding and rigid foundations, Mechanics of Advanced Materials and Structures 26 (2019) 107–118. doi:10.1080/15376494.2017.1365978.

[15] J. Chen, J. Yu, L. Elmaimouni, B. Zhang, H. Tu, Rayleigh waves in viscoelastic piezoelectric half-space with cladding structures: An analytic legendre-laguerre polynomial method, European Journal of Mechanics - A/Solids 107 (2024) 105397. doi:https://doi.org/10.1016/j.euromechsol.2024.105397.

[16] M. Biswas, S. A. Sahu, On the rayleigh wave velocity in n-type piezoelectric semiconductors with enhanced flexoelectricity, Mathematics and Mechanics of Solids 30 (2025) 2822–2842. doi:10.1177/10812865251315937.

[17] S. Saha, S. Pramanik, N. Pradhan, S. K. Samal, Rayleigh-type surface waves in transversely isotropic and soil layered structure: A potential-based modelling approach, Mathematics and Mechanics of Solids 0 (2026) 10812865251409145. doi:10.1177/10812865251409145.

[18] S. Saha, A. K. Singh, A. Chattopadhyay, Rayleigh-type wave propagation in exponentially graded initially stressed composite structure resting on rigid and yielding foundations, Applied Mathematics and Computation 435 (2022) 127421. doi:https://doi.org/10.1016/j.amc.2022.127421.

[19] S. Manna, T. Anjali, Rayleigh type wave dispersion in an incompressible functionally graded orthotropic half-space loaded by a thin fluid-saturated aeolotropic porous layer, Applied Mathematical Modelling 83 (2020) 590–613. doi:https://doi.org/10.1016/j.apm.2020.02.007.

[20] J.-W. Zhao, L.-Y. Yao, X.-D. Zhang, H. Chen, Investigation of elastic waves frequency converted for the piezoelectric metamaterial cylindrical shell, Composite Structures 354 (2025) 118799. doi:https://doi.org/10.1016/j.compstruct.2024.118799.

[21] R. Kumari, A. K. Singh, Rayleigh wave in a piezoelectric micro-mechanical bi-material system with mechanically and dielectrically imperfect interfaces, Waves in Random and Complex Media 0 (2023) 1–20. doi:10.1080/17455030.2023.2205966.

[22] B. Paswan, P. Singh, S. A. Sahu, Mathematical study for the rayleigh wave propagation in a composite structure with piezoelectric material, Journal of Solid Mechanics 15 (2023) 144–159.

[23] A. K. Singh, P. Rajput, S. Guha, S. Singh, Propagation characteristics of love-type wave at the electro-mechanical imperfect interface of a piezoelectric fiber-reinforced composite layer overlying a piezoelectric half-space, European Journal of Mechanics - A/Solids 93 (2022) 104527. doi:https://doi.org/10.1016/j.euromechsol.2022.104527.

[24] S. Guha, A. Kumar Singh, Effects of initial stresses on reflection phenomenon of plane waves at the free surface of a rotating piezothermoelastic fiber-reinforced composite half-space, International Journal of Mechanical Sciences 181 (2020) 105766. doi:https://doi.org/10.1016/j.ijmecsci.2020.105766.

[25] S. Guha, A. K. Singh, Plane wave reflection/transmission in imperfectly bonded initially stressed rotating piezothermoelastic fiber-reinforced composite half-spaces, European Journal of Mechanics - A/Solids 88 (2021) 104242. doi:https://doi.org/10.1016/j.euromechsol.2021.104242.

[26] A. Srivastava, S. Mukhopadhyay, Size dependency and dual phase-lag effects on thermoelastic damping of a piezothermoelastic thin rectangular kirchhoff plate, Journal of Thermal Stresses 48 (2025) 1771–1791. doi:10.1080/01495739.2025.2485469.

[27] J. Lou, Z. Xiao, H. Fan, X. Fang, T. Shen, J. Du, Suppression and mode conversion of rayleigh-type surface acoustic waves by piezoelectric metamaterials, Composite Structures 372 (2025) 119531. doi:https://doi.org/10.1016/j.compstruct.2025.119531.

[28] A. Srivastava, O. N. Shivay, S. Mukhopadhyay, On temperature-rate-dependent two-temperature piezothermoelasticity theory: On temperature-rate-dependent two-temperature..., Z. Angew. Math. Phys. 76 (2025). doi:10.1007/s00033-025-02638-z.

[29] M. Bhat, S. Manna, Hybrid rayleigh wave along a nonlocal nonlinear metasurface with two-degree-of-freedom spring–mass resonators, European Journal of Mechanics - A/Solids 104 (2024) 105214. doi:https://doi.org/10.1016/j.euromechsol.2023.105214.

[30] M. Bhat, S. Manna, M. Alkinidri, Rayleigh wave fields in a multilayered micropolar media, International Journal of Geomechanics 24 (2024) 04024026. doi:10.1061/IJGNAI.GMENG-8725.

[31] M. Bhat, S. Manna, On different modes of rayleigh wave fields in a micropolar nonlocal viscoelastic medium, ZAMM - Journal of Applied Mathematics and Mechanics / Zeitschrift für Angewandte Mathematik und Mechanik 105 (2025) e202400604. doi:https://doi.org/10.1002/zamm.202400604.

[32] M. Mahanty, A. Chattopadhyay, S. Dhua, M. Chatterjee, Propagation of shear waves in homogeneous and inhomogeneous fibre-reinforced media on a cylindrical earth model, Applied Mathematical Modelling 52 (2017) 493–511. doi:https://doi.org/10.1016/j.apm.2017.07.061.

[33] A. Nath, S. Dhua, S. Mondal, An investigation of torsional surface wave in a piezoelectric fiber-reinforced composite layer imperfectly bonded to a functionally graded half-space, European Journal of Mechanics - A/Solids 104 (2024) 105210. doi:https://doi.org/10.1016/j.euromechsol.2023.105210.

[34] A. Nath, S. Dhua, Sh-wave scattering at the boundary between two piezoelectric half-spaces with surface-interface energy, Journal of Engineering Mechanics 151 (2025) 04025021.

[35] S. Dhua, S. Mondal, A. Maji, Surface effects on wave propagation in piezoelectric–piezomagnetic loosely bonded bilayer system using nonlocal theory of elasticity, Thin-Walled Structures 197 (2024) 111612. doi:https://doi.org/10.1016/j.tws.2024.111612.

[36] N. Pradhan, S. Manna, S. Samal, S. Saha, Sh wave in two-layered structure of functionally graded viscoelastic and monoclinic media under the influence of an interior point source, The European Physical Journal Plus 140 (2025). doi:10.1140/epjp/s13360-025-06086-6.

[37] G. Murty, A theoretical model for the attenuation and dispersion of stoneley waves at the loosely bonded interface of elastic half spaces, Physics of the Earth and Planetary Interiors 11 (1975) 65–79.

[38] S. Rokhlin, Y. Wang, Analysis of boundary conditions for elastic wave interaction with an interface between two solids, The Journal of the Acoustical Society of America 89 (1991) 503–515. doi:10.1121/1.400374.

[39] A. I. Lavrentyev, S. Rokhlin, Ultrasonic spectroscopy of imperfect contact interfaces between a layer and two solids, The Journal of the Acoustical Society of America 103 (1998) 657–664. doi:10.1121/1.423235.

[40] A. D. Sharmistha Rakshit, Kshitish Ch. Mistri, A. Lakshman, Effect of interfacial imperfections on sh-wave propagation in a porous piezoelectric composite, Mechanics of Advanced Materials and Structures 29 (2022) 4008–4018. doi:10.1080/15376494.2021.1916138.

[41] A. K. Singh, P. Rajput, S. Guha, S. Singh, Propagation characteristics of love-type wave at the electro-mechanical imperfect interface of a piezoelectric fiber-reinforced composite layer overlying a piezoelectric half-space, European Journal of Mechanics-A/Solids 93 (2022) 104527.

[42] B. Dholey, A. Alneamy, K. Mistri, S. Guha, M. Tharwan, The influence of sh-wave propagation in a tri-layered composite structure with interfacial imperfections, Journal of Vibration Engineering & Technologies 13 (2025) 197. doi:https://doi.org/10.1007/s42417-025-01776-y.

[43] B. Dholey, K. Mistri, Shear-horizontal wave dynamics in smart fiber composites with layerwise interfacial imperfections, Boletim da Sociedade Paranaense de Matemática 43 (2025). doi:10.5269/bspm.77807.

[44] R. Kumari, S. Kumar, Spring-membrane models to study love-type surface wave in smart composite structure: A comparative analysis, International Journal of Engineering Science 209 (2025) 104225. doi:https://doi.org/10.1016/j.ijengsci.2025.104225.

[45] C. Q. Su, P. Guo, Y. Y. Wang, G. D. Zhang, Internal friction analysis for the viscoelastic constitutive models, IOP Conference Series: Earth and Environmental Science 188 (2018) 012030. URL: https://doi.org/10.1088/1755-1315/188/1/012030. doi:10.1088/1755-1315/188/1/012030.

[46] S. Saha, A. K. Singh, A. Chattopadhyay, On propagation behavior of sh-wave and rayleigh-type wave in an initially stressed exponentially graded fiber-reinforced viscoelastic layered structure, Waves in Random and Complex Media 31 (2021) 486–514. doi:10.1080/17455030.2019.1599147.

[47] S. Guha, A. K. Singh, Transference of sh waves in a piezoelectric fiber-reinforced composite layered structure employing perfectly matched layer and infinite element techniques coupled with finite elements, Finite Elements in Analysis and Design 209 (2022) 103814. doi:https://doi.org/10.1016/j.finel.2022.103814.

[48] A. Kumar, D. Chakraborty, Effective properties of thermo-electro-mechanically coupled piezoelectric fiber reinforced composites, Materials & Design 30 (2009) 1216–1222. doi:https://doi.org/10.1016/j.matdes.2008.06.009.

[49] M. M. Amin, A. M. A. A. Nasr, A. A. El-Bary, S. M. Abo-Dahab, Propagation of surface waves in generalized thermoelastic media under influence of magnetic field and rotation and its applications in engineering and geophysics, Mechanics Based Design of Structures and Machines 50 (2022) 3417–3440. doi:10.1080/15397734.2020.1804934.

[50] X.-K. Xia, H.-S. Shen, Nonlinear vibration and dynamic response of fgm plates with piezoelectric fiber reinforced composite actuators, Composite Structures 90 (2009) 254–262. doi:https://doi.org/10.1016/j.compstruct.2009.03.018.

[51] L. Zhang, J. Zhao, G. Nie, et al., Propagation of rayleigh-type surface waves in a layered piezoelectric nanostructure with surface effects, Applied Mathematics and Mechanics (English Edition) 43 (2022) 327–340. URL: https://doi.org/10.1007/s10483-022-2824-7. doi:10.1007/s10483-022-2824-7.

[52] J. D. Achenbach, Wave Propagation in Elastic Solids, North-Holland, Amsterdam, 1973.

Appendix A. Effective complex constants (SM/RM)

All constituent constants c^f_{ij}, c^q_{ij}, e^f_{ij}, ε^f_{ij}, ε^q_{ij} are the complex constants of Eq. (2) evaluated at ω, with Eq. (6) (in particular $e^f_{32} = e^f_{31}$); $V_q = 1 - V_f$.

$$S_1 = c^f_{13} - c^q_{13}, \qquad S_2 = c^f_{12} - c^q_{12}, \qquad S_3 = V_q c^f_{23} + V_f c^q_{23},$$

$$S_4 = V_q c^f_{33} + V_f c^q_{33}, \qquad S_5 = V_q c^f_{22} + V_f c^q_{22}, \qquad S_6 = V_q c^f_{55} + V_f c^q_{55}, \qquad S_7 = V_q c^f_{44} + V_f c^q_{44},$$

$$\gamma_1 = V_q S_1 S_3 - V_q S_2 S_4, \qquad \gamma_2 = c^q_{23} S_4 - c^q_{33} S_3, \qquad \gamma_3 = V_q e^f_{32} S_4 - V_q e^f_{33} S_3,$$

$$\gamma_4 = -V_q S_1 S_5 + V_q S_2 S_3, \qquad \gamma_5 = -c^q_{23} S_3 + c^q_{33} S_5, \qquad \gamma_6 = -V_q e^f_{32} S_3 + V_q e^f_{33} S_5,$$

$$\Lambda_1 = V_f S_2, \qquad \Lambda_2 = V_f S_1, \qquad \Phi = S_4 S_5 - S_3^2,$$

$$c_{11} = V_f c^f_{11} + V_q c^q_{11} + (\gamma_1 \Lambda_1 + \gamma_4 \Lambda_2)/\Phi,$$

$$c_{13} = c^f_{13} + (\gamma_1 c^f_{23} + \gamma_4 c^f_{33})/\Phi,$$

$$c_{33} = (\gamma_2 c^f_{23} + \gamma_5 c^f_{33})/\Phi, \qquad c_{44} = c^f_{44} c^q_{44}/S_7, \qquad c_{55} = c^f_{55} c^q_{55}/S_6,$$

$$e_{31} = V_f e^f_{31} - (\gamma_3 \Lambda_1 + \gamma_6 \Lambda_2)/\Phi,$$

$$e_{33} = e^f_{33} - (\gamma_3 c^f_{23} + \gamma_6 c^f_{33})/\Phi,$$

$$e_{15} = e^f_{15}\left[1 - \frac{V_q c^f_{55}}{S_6}\right] = \frac{V_f e^f_{15} c^q_{55}}{S_6},$$

$$\varepsilon_{11} = V_f \varepsilon^f_{11} + V_q \varepsilon^q_{11} + \frac{V_f V_q (e^f_{15})^2}{S_6},$$

$$\varepsilon_{33} = V_f \varepsilon^f_{33} + V_q \varepsilon^q_{33} + V_f \frac{\gamma_3 e^f_{32} + \gamma_6 e^f_{33}}{\Phi}.$$

The numerator of c_{13} contains γ_1 and γ_4 (not γ_2). For transversely isotropic constituents $c_{55} = c_{44}$, which is the shear constant in Eqs. (13)–(14). Setting all relaxation times to zero recovers the elastic PFRC expressions. These formulas reproduce exactly the direct solution of Eqs. (8)–(10), satisfy the reciprocity $c_{13} = c_{31}$ and the identity of e_{31} obtained from τ_{11} and from D_3, and return the matrix (fiber) constants for $V_f = 0$ ($V_f = 1$).